



The Role of O₂ and H₂O Impurities in Dictating the Oxidation Mechanism and Protective Capacity of 9Cr Steels in Hot CO₂

F. Rouillard¹ · F. Jomard² · L. Latu-Romain³ · L. Martinelli¹ · F. Miserque¹ · D. J. Young⁴

Received: 29 July 2023 / Revised: 24 August 2023 / Accepted: 28 August 2023 /
Published online: 19 September 2023

© The Author(s), under exclusive licence to Springer Science+Business Media, LLC, part of Springer Nature 2023

Abstract

The initial stages of oxidation of 9Cr steel in CO₂, O₂, CO₂–O₂ and CO₂–O₂–H₂O is studied by gas phase analysis (GPA) at 550 °C using ¹³C^{16,16}O₂, ^{18,18}O₂ and ²H₂¹⁶O isotopic molecules in order to discriminate the reactions of all gas molecules. Protective and non-protective oxide scales are formed on 9Cr steel depending on the exact composition of the gas mixture. In pure CO₂, 9Cr steel forms a slow growing chromium-rich oxide scale without any carburization. Adding O₂ impurities in CO₂ favors the formation of fast growing iron-rich duplex oxide scale coupled to strong carburization. Adding several % of O₂ in CO₂ favors again the formation of slow growing oxide scale but with different structure and composition than in pure CO₂. GPA analyses combined with oxide scale analyses demonstrate that the composition and structure of the transient oxide scale formed on 9Cr surface is determined by the rate at which surface adsorbed oxygen atoms are supplied by the gas phase in the first minutes of exposure. The presence of the very oxidizing O₂ molecules in CO₂ increases drastically the surface oxidation rate, favoring formation of a non-protective oxide scale which transmits carbon permitting carburization of the steel. Adding water vapor to a CO₂ gas environment slows carburization. Preferential adsorption of water vapor molecules over CO₂/CO molecules in the inner oxide scale is proposed to explain this result. A unified mechanism for the formation of the transient oxide scale on 9Cr steel in CO₂/O₂/H₂O gas mixtures is described.

Keywords Oxidation · Carbon dioxide · Oxygen · Water vapor · Chromium steel

Introduction

Ferritic-martensitic steels are widely used at moderate temperatures where good creep strength and acceptable corrosion resistance are required. However, their chromium levels are marginal, and service in CO₂-rich gases can lead to two very different outcomes: formation of a protective Cr-rich oxide scale or non-protective iron-rich oxide scale sometimes called «breakaway corrosion» [1]. In the latter case, a much thicker, duplex scale consisting of an outer layer of almost pure iron oxide and an inner porous layer of spinel (Fe_{3-x}Cr_xO₄) with iron oxide results, and carburization of the underlying metal is extensive. As the same steel can produce the two different results at the same temperature in different CO₂ gases, reasons for the difference are sought in the details of gas composition.

Commercial purity CO₂ contains of order 10 ppm (by volume) O₂, whereas high purity CO₂ contains about 1 ppm. On the other hand, flue gases resulting from carbon combustion contains several % O₂, because excess oxygen is used to ensure maximum fuel utilization. Work by Bouhieda et al. [2, 3] showed that a 12 Cr ferritic-martensitic steel VM12 (all alloy compositions in wt. %) exposed at 550 °C to high purity CO₂ containing less than 1 ppm O₂ developed a thin, protective, Cr-rich oxide scale, but when the gas was commercial purity CO₂ (measured O₂ content of 70 ppm), the thicker duplex scale morphology resulted.

The opposite effect was observed at higher oxygen levels (1–3 vol %). Exposure of a 9Cr ferritic-martensitic steel to Ar–50CO₂–(1–3)O₂ at 550 °C led to partial passivation of the steel surface [4]. A thin, protective Cr-rich scale formed on parts of the surface in 1% O₂ and most of the surface was passivated in this way in a 3% O₂ gas. The remainder of the surface grew thick duplex scales. The authors noted that a full explanation was not available. Similar results have been reported by others [5–7].

Finally, it has been observed that the presence of a few % of H₂O in CO₂ decreased the carburization rate of 9Cr drastically at 550 °C [8] and 650 °C [9].

As is seen, breakaway corrosion during steel exposure to CO₂ is at least partially suppressed by high oxygen partial pressures, is promoted by low oxygen levels and again suppressed by very low level of oxygen. This puzzling result remains to be explained. Interpretation is made difficult by the low temperatures involved, and the consequently slow approach to local thermodynamic equilibrium in solids.

The issue is of practical importance because CO₂ is used as a heat transfer medium in a number of applications. Pressurized CO₂ is the primary coolant in the British AGR reactors. Supercritical CO₂ is proposed as the working fluid in a Brayton cycle, where the heat source can be concentrated solar power or a new generation nuclear reactor. Oxyfuel combustion of fossil fuels produces flue gases made up mainly of CO₂, H₂O and O₂.

For economic reasons, the gas used in all cases will be commercial purity, i.e., containing some tens of ppm O₂. In closed systems such as the AGR or Brayton cycle, any impurity oxygen in the gas is removed by reaction with containment

materials, and graphite in the case of the AGR. Thus the additional question arises as to how long the deleterious effect of impurity O_2 lasts.

It seems likely that the initial transient stages of gas-steel reaction are important in establishing the reaction morphology and nature of the reaction products. This is a difficult domain to study using conventional methods of reaction product characterization. However, reaction kinetics can be followed in the very early stages by observing changes in the gas phase compositions using mass spectrometric analysis and isotopically labelled gases. This technique has recently been shown [10] to be able to distinguish the contributions to corrosion of the oxygen and CO_2 species.

This paper is mainly concerned with the early stages of corrosion for a 9Cr ferritic-martensitic steel exposed to CO_2 containing different levels of O_2 and pure O_2 . Reaction kinetics are followed using gas phase analysis (GPA) in a closed system, coupled with subsequent analysis of reaction products and the underlying steel. Additional results are added on the effect of H_2O in CO_2 .

Corrosion Studies Using Gas Phase Analysis Technique (GPA)

Experimental Apparatus

The experiments were conducted in a gas phase analysis facility (GPA) described in detail in [10]. This apparatus consisted of three main parts: An almost completely closed reaction chamber, a gas handling system and a mass spectrometer (MS) placed in an ultra-high vacuum (UHV) chamber. The reaction chamber consisted of a 0.4 m long silica tube connected to a stainless steel cross. The total volume of the reaction chamber was about 200 cm^3 . Silica tube was chosen as the tube material because it showed negligible reactivity and gas release during operation. One end of the tube was externally heated by a moving furnace positioned on a rail. The isothermal zone length ($\pm 5\text{ }^\circ\text{C}$) was measured to be about 4 cm which is larger than the sample length.

One branch of the stainless steel cross connected to quartz tube was connected via a leak valve to an UHV chamber containing the MS. The UHV chamber was pumped with a turbo-molecular pump down to 10^{-9} mbar. During experiment, the leak valve was slightly opened to transmit small quantities of reaction chamber gas to the mass spectrometer. Under the conditions used, the mass spectrometer yielded a linear response to the partial pressures of all gas species in the UHV chamber and in the reaction chamber. The linear coefficients for CO_2 and O_2 molecules were obtained at the beginning of each experiment before reaction of the gas phase with the sample. The sensitivity and measurement accuracy for gas partial pressures was improved by using a direct connection from the leak valve to the ionization chamber in the MS. The total pressure of the reaction chamber could be measured at room temperature by three absolute capacitive pressure gauges (full scale: 1 mbar, 10 mbar and 100 mbar) fitted on the stainless steel cross part of the reaction chamber.

Table 1 Composition of the gas mixtures used in the corrosion tests

mbar/Test name	1CO ₂	49CO ₂	49CO ₂ /1O ₂	1O ₂	15O ₂	10H ₂ O–1O ₂	10CO ₂ –1O ₂ –x ² H ₂ O
P _{CO₂}	1	49	49	–	–	–	10
P _{O₂}	–	–	1	1/	15/	1	1
P _{H₂O}	–	–	–	–	–	10	x = 1, 5, 10
Exposure duration (min)	240	240	20 or 240	20	20	240	20 or 240

Table 2 Composition of 9Cr steel

wt%	Trade Name	Fe	C	Cr	Mo	Mn	Si	Ni	Al
9Cr steel	EM10	Balance	0.1	9	0.96	0.49	0.41	0.05	0.004

The remaining branch of the stainless steel cross of the reaction chamber was connected to a gas handling system. This provided controlled inlet of isotopic gas molecules in the reaction chamber. A bottle of ^{18,18}O₂, a bottle of ¹³C^{16,16}O₂ and a tank of ²H₂¹⁶O liquid were connected. Their exact isotopic composition were measured by MS. The ^{18,18}O₂ bottle contained about 12 vol% of ^{16,18}O₂ molecules, the ¹³C^{16,16}O₂ bottle about 1 vol% of ¹³C^{16,18}O₂ as main impurity. The used ²H₂¹⁶O was composed of 60 vol% of ^{2,2}H₂¹⁶O and 40 vol% of ^{2,1}H₂¹⁶O molecules. The isotopic carbon and oxygen composition of the two bottles was chosen in order to differentiate by MS in the gas phase or subsequent SIMS analyses of the sample surface, oxygen atoms coming from O₂ molecules (¹⁸O) from oxygen atoms coming from CO₂ molecules (¹⁶O) and carbon atoms coming from the metallic sample (¹²C) from carbon atoms coming from CO₂ molecules (¹³C). The use of deuterated water ^{2,x}H₂O was used to favor hydrogen detection by mass spectrometry both in the gas phase GPA and during analysis of the sample by SIMS.

After verifying that there was negligible background interference and negligible gas consumption due to sampling though the leak valve, the GPA facility was used to measure both consumption and production of gas molecules during reaction of steel.

Experimental Procedure

The interaction of 9Cr steel samples with CO₂–O₂ gas mixtures was studied at 550 °C in a total gas pressure between 1 and 50 mbar. Compositions of gas mixtures used in this study are summarized in Table 1, with absolute pressures quoted for room temperature.

The elemental composition of 9Cr steel (EM10 grade) is given in Table 2.

Samples of dimension 20×9×0.1 mm were cut by electrical discharge machining from thicker EM10 grade plate. Due to the low sample thickness and because no

additional strain hardening of the surface was wanted, no mechanical polishing of the sample surfaces was carried out, and they were all exposed in their as-received state. The roughness of the sample surface was measured by laser interferometer. The average roughness was about 1 μm with 15 μm deep zones induced by the electrical discharge machining process. After ultrasonic cleaning in ethanol, each sample was weighed then inserted into the reaction chamber via a gate valve and positioned in the colder zone of the reaction chamber near the stainless steel cross. Then, the reactor was pumped down to 10^{-7} mbar at room temperature, the gas mixture injected at the desired pressure, the reactor heated to 550 $^{\circ}\text{C}$ and the sample moved into the hot zone. More details about the used experimental procedure is given in [10]. During each experiment, the evolution of the gas phase composition was measured by MS and the total gas pressure in the reaction chamber was measured by capacitive gauges. In particular, all mass/charge (m/z) ratios corresponding to CO , CO_2 , H_2 , H_2O and O_2 molecules composed of ^{13}C , ^{12}C , ^2H , ^{16}O and ^{18}O atoms were carefully followed. After reaction, the corroded sample were weighed and metallographically sectioned. The morphology, composition and structure of the corrosion products formed on the sample surface and deeper in the substrate were analyzed by various analytical techniques such as: X-Ray Photoelectron Spectroscopy (with or without sputtering mode, XPS), Glow Discharge Optical Emission Spectroscopy (GDOES), Raman spectroscopy, optical microscopy (OM), scanning electron microscopy (SEM) with EDS detection and transmission electron microscopy (TEM) with EDS spectroscopy and TEM-ASTAR mode [11] for a few selected samples on thin lamellae prepared by dual FIB-SEM microscopy.

The isotopic oxygen, carbon and hydrogen composition of the corroded surface were obtained on a few samples by SIMS (CAMECA IMS 7F model). To optimize their detection, negative ion detection mode was selected. The surface was scanned over $150 \times 150 \mu\text{m}^2$ by primary Cs^+ ions with an impact energy of 15 keV and a primary beam intensity of 40 nA. The diameter of the analyzed area in the center of the sputtered zone was 33 μm . High mass resolution mode was used ($M/\Delta M = 4000$) in order to distinguish between atomic and molecular species detected at a very close mass to charge ratio, in particular $^{13}\text{C}^-/^{12}\text{C}^1\text{H}^-$ and $^{18}\text{O}^-/^{16}\text{OH}_2^-$.

Results

Corrosion in Pure CO_2

1CO_2

Exposure of 9Cr steel to 1 mbar CO_2 for 240 min at 550 $^{\circ}\text{C}$ produced a golden colored sample surface. Consumption of $^{13}\text{C}^{16,16}\text{O}_2$ and formation of $^{13}\text{C}^{16}\text{O}$ molecules were observed (Fig. 1). Simultaneously, the formation of $^{12}\text{C}^{16}\text{O}$ was detected. The formation of $^{12}\text{C}^{16}\text{O}$ proved that decarburization of the sample occurred through the reaction (R1) as proposed for mild steel exposed to CO_2 [5]:

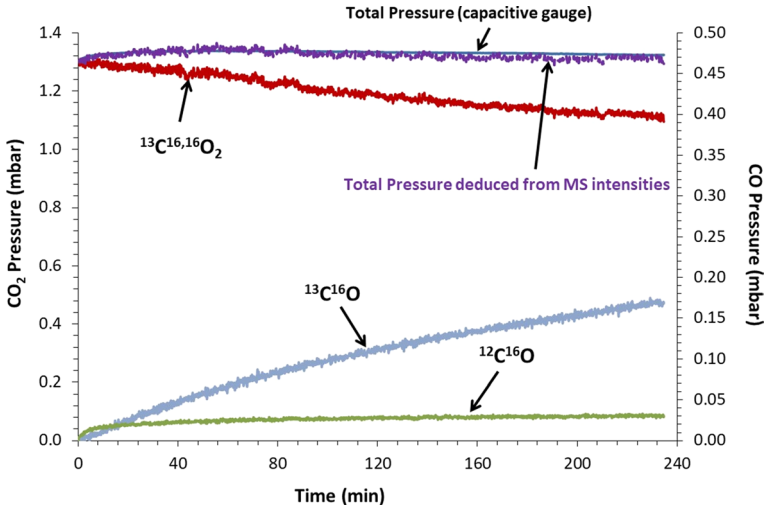
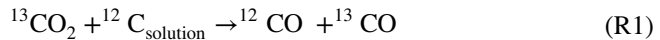


Fig. 1 Gas phase composition measured by MS during corrosion test 1CO₂ for 240 min



This decarburization reaction was transient since the production of $^{12}\text{C}^{16}\text{O}$ was observed only during the first minutes of exposure. Since the production rate of ^{13}CO was much higher than that of ^{12}CO , a large part of the ^{13}CO was produced by steel oxidation according to (R2).

Analyses of 9Cr steel surface by XPS in sputtering mode (Fig. 2) revealed the formation of a thin chromium-rich oxide layer enriched slightly with aluminum and manganese (about 5 at%, not shown in Fig. 2). The presence of metallic Cr and Fe in the oxide layer was due to the uneven oxide/metal interface during the sputtering of the 2 mm × 2 mm² surface by XPS.

The (Cr/Fe + Cr) molar ratio in the oxide layer was about 70 at%. The ionization degree of chromium and iron at the gas interface was analyzed by XPS (not shown). All chromium ions were Cr³⁺ and about 80% of iron ions were Fe³⁺, the other part being Fe²⁺. This composition suggests the formation of M₂O₃ with M being mainly chromium on the major part of the surface. The formation of Cr-rich M₂O₃ has been confirmed by Raman spectroscopy (not shown). From a GDOES profile (not shown), the oxide thickness was estimated to be lower than 50 nm which was in good agreement with the measured $^{13}\text{CO}^{16}$ molecule production. Thus, it was proposed that for 1CO₂ test, an oxide scale grew on the surface through the following reaction (R2):

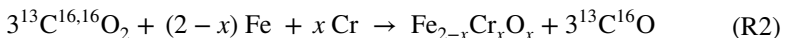
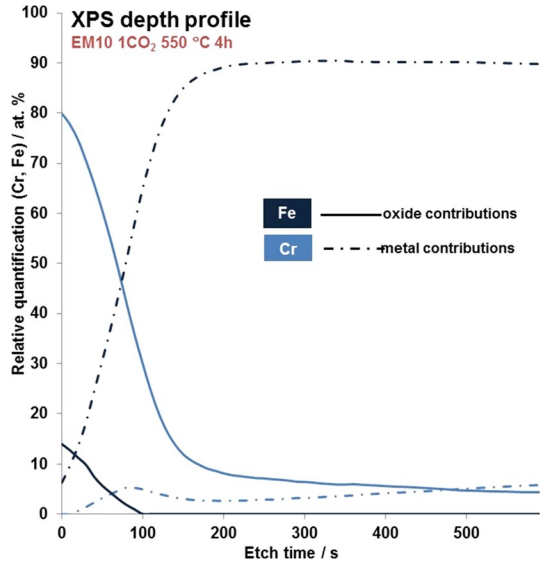


Fig. 2 Elementary profiles of 9Cr sample surface by XPS in sputtering mode after corrosion test 1CO₂ for 240 min



49CO₂

Changes in gas composition during exposure of 9Cr steel in a higher pressure of CO₂, 49 mbar, at 550 °C for 240 min are shown in Fig. 3. When moving the furnace over the reactor, the initial pressure of CO₂ increased to 60 mbar.

As observed in Fig. 3, the ¹³C¹⁶,¹⁶O₂ (*m/z* = 45) pressure decreased slowly, ¹³C¹⁶O (*m/z* = 29) formed simultaneously and the total pressure in the reactor stayed constant. After reaction, the 9Cr steel surface was slightly darkened. XPS analysis in

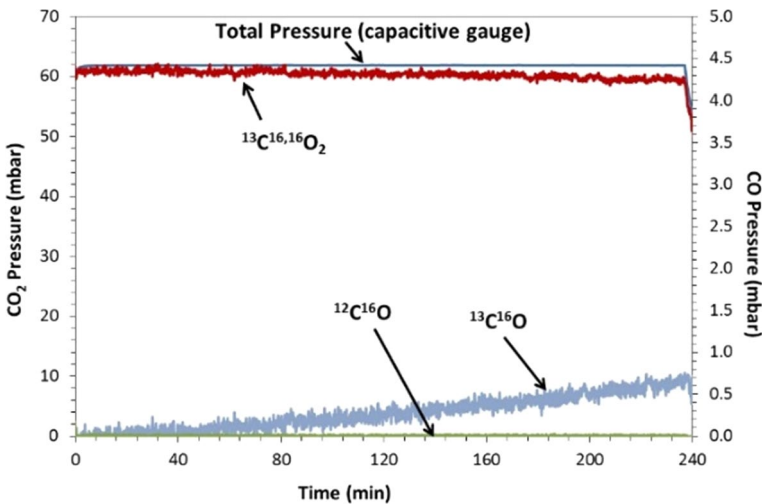


Fig. 3 Gas phase composition measured by MS during corrosion test 49CO₂ for 240 min

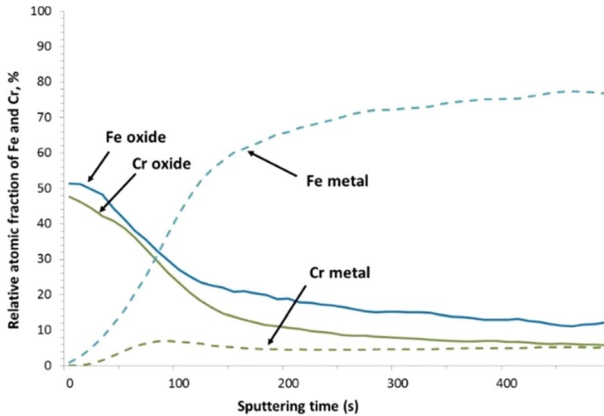


Fig. 4 Oxidized and metallic iron and chromium profiles measured by XPS (sputtering mode) through 9Cr steel surface after corrosion test 49CO₂ for 240 min

sputtering mode revealed that a thin 50 at% chromium—50 at% iron bearing oxide layer formed on the surface (Fig. 4). The oxide thickness was estimated from the measured mass gain to be about 250 nm. The Cr enrichment within the oxide layer was lower than the 80 at% of Cr enrichment obtained after exposure in 1 mbar CO₂ and the oxide thickness higher.

This time, the oxide layer was identified as Cr-rich Fe–Cr spinel oxide by Raman spectroscopy (not shown). According to Fig. 4, the following average stoichiometry can be proposed: Fe_{1.5}Cr_{1.5}O₄. On the basis of the gas phase analysis, the steel oxidation reaction (R3) can be formulated as

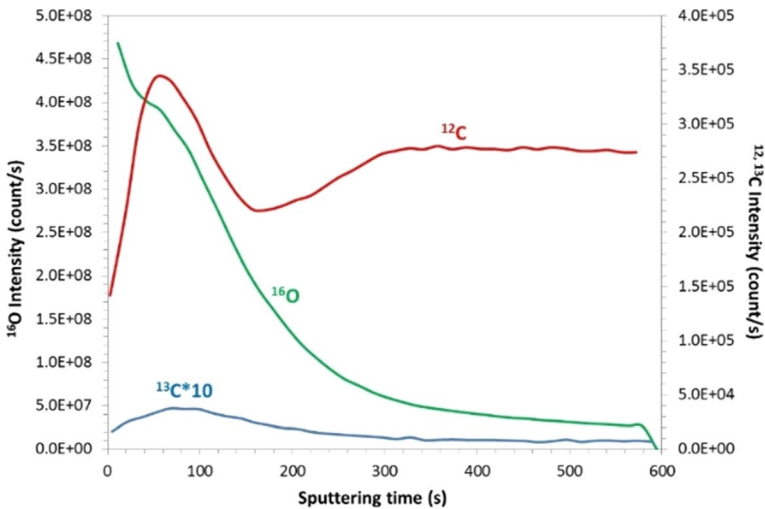


Fig. 5 Oxygen and carbon profiles measured by SIMS on 9Cr steel surface after corrosion test 49CO₂ for 240 min. The ¹³C intensity was multiplied by 10

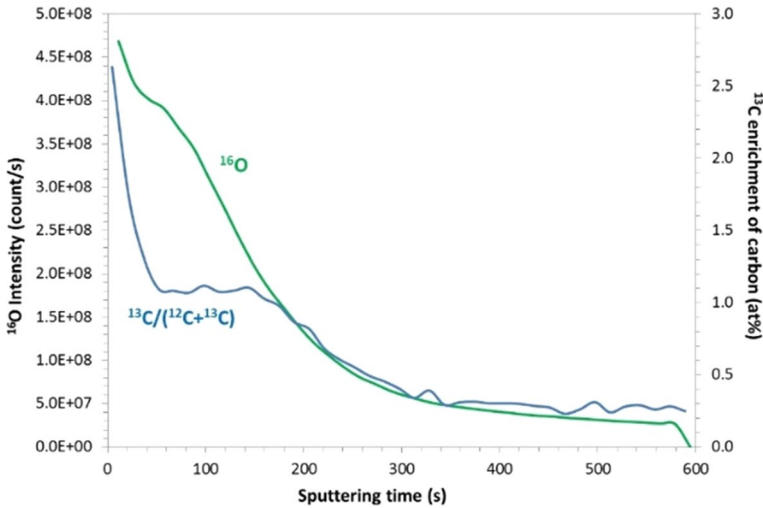
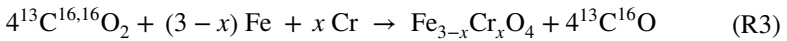


Fig. 6 Oxygen profile and ¹³C enrichment of carbon (at%) measured by SIMS on 9Cr surface after corrosion test 49CO₂ for 240 min



The oxygen/carbon profiles and the ¹³C enrichment profile in the 9Cr sample surface were measured by SIMS and are shown in Figs. 5 and 6, respectively. A slight depletion of ¹²C is detected below the oxide layer in good agreement with the GDOES profile (not shown). In order to detect any transfer of ¹³C coming from ¹³CO₂ molecules, the ¹³C intensity due to the initial presence of carbon in unreacted 9Cr steel (natural isotopic abundance ratio ¹³C/(¹²C + ¹³C) = 1.1 at%) was measured in a reference sample and subtracted from the ¹³C intensity measured in the corroded sample. ¹³C was detected in the reacted sample, both in the oxide layer and below the oxide scale. However, its concentration was extremely low, and it could be only detected as a result of the high carbon sensitivity of the SIMS apparatus. By considering that the intensity of ¹²C measured in the metallic bulk (around 2.7 × 10⁵ count/s) corresponds to 0.1 wt%, it is concluded that only a few tens of ppm by weight of ¹³C were transferred below the oxide scale during reaction with 49CO₂.

Corrosion in CO₂ with Low Concentrations of O₂ (Low P_{O₂}/P_{CO₂} Ratio)

49CO₂/10O₂ for 240 min

The evolution of the gas phase composition during the exposure of 9Cr steel in 49 mbar ¹³C^{16,16}O₂ + 1 mbar ^{18,18}O₂ at 550 °C is shown in Fig. 7.

Two stages could be distinguished: stage 1 during the first 10 min and stage 2 from 10 min to the end of the experiment (zoom in Fig. 8). During the first stage, ^{18,18}O₂ molecules were consumed, ¹³C^{16,16}O₂ molecules were consumed and

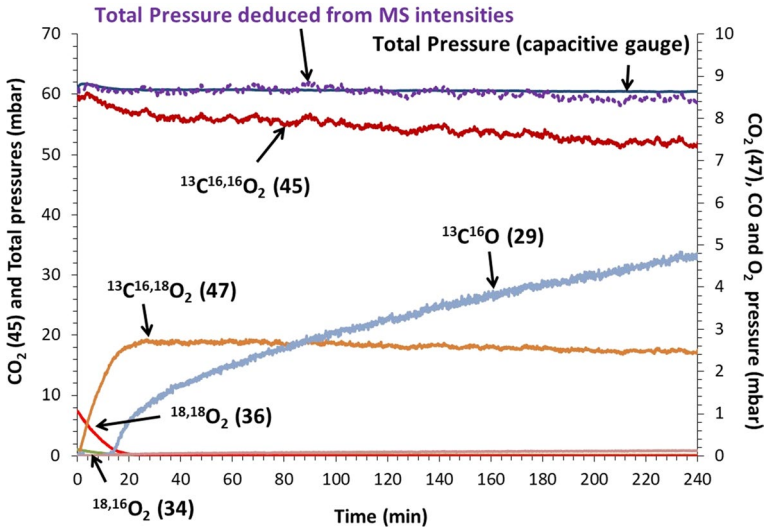


Fig. 7 Gas phase composition measured by MS during corrosion test $49\text{CO}_2/10\text{O}_2$ at $550\text{ }^\circ\text{C}$ for 240 min. The values in brackets correspond to the mass to charge ratio

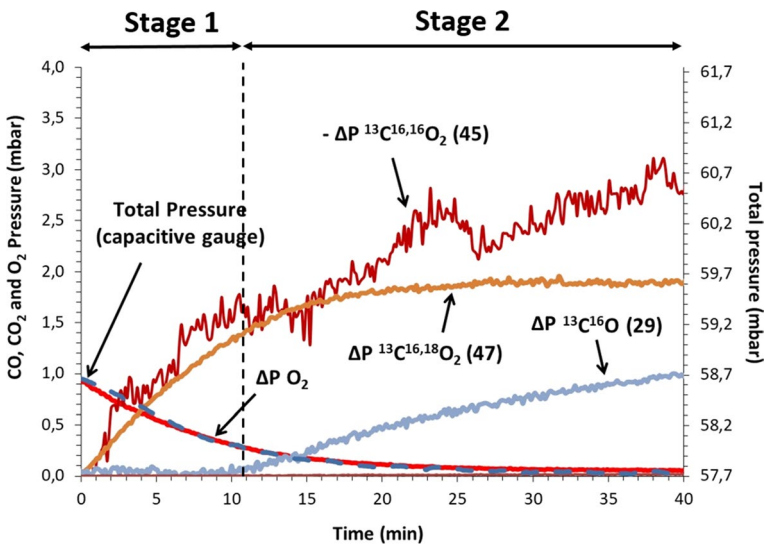


Fig. 8 Evolution of the pressure of all molecules during corrosion test $49\text{CO}_2/10\text{O}_2$ for 240 min. Note: The evolution of $^{13}\text{C}^{16,16}\text{O}_2$ (45) pressure is shown in absolute values since it was negative (consumed in Fig. 7)

$^{13}\text{C}^{16,18}\text{O}_2$ molecules were produced. As shown in Fig. 8, the production rate of $^{13}\text{C}^{16,18}\text{O}_2$ at this stage was equal to the consumption rate of $^{13}\text{C}^{16,16}\text{O}_2$. No ^{13}CO was produced in the gas phase during this first stage. Then, after 10 min, once the

pressure of $^{18,18}\text{O}_2$ has decreased below 0.3 mbar in the reactor chamber, ^{13}C started to be produced accompanied by the consumption of $^{13}\text{C}^{16,16}\text{O}_2$ molecules.

These observations were very similar to those made during exposure of mild steel and iron in CO_2/O_2 gas mixtures [5]. It was proposed in [5] that $^{13}\text{C}^{16,16}\text{O}_2$ and $^{18,18}\text{O}_2$ adsorb on the surface. Subsequently, $^{13}\text{C}^{16,16}\text{O}_2$ molecules dissociate to form adsorbed ^{16}O and $^{13}\text{C}^{16}\text{O}$, and $^{18,18}\text{O}_2$ molecules dissociate to form two adsorbed atoms of ^{18}O . These ^{18}O atoms either react with the metallic elements to form and grow oxide or combine with adsorbed $^{13}\text{C}^{16}\text{O}$ molecules to form $^{13}\text{C}^{18,16}\text{O}_2$ gas species (similarly with $^{13}\text{C}^{18}\text{O}$ formed by $^{13}\text{C}^{18,18}\text{O}_2$ dissociation to form $^{13}\text{C}^{18,18}\text{O}_2$).

In order to know which proportion of ^{18}O provided by the dissociation reaction of $^{18}\text{O}_2$ reacted with $^{13}\text{C}^{16}\text{O}$ to form $^{13}\text{C}^{16,18}\text{O}_2$ or oxidised metal, the production rate of $m/z=47$ ($^{13}\text{C}^{16,18}\text{O}_2$) and loss rates of $m/z=36$ ($^{18,18}\text{O}_2$) were compared. The absolute value of the rate ratio is shown in Fig. 9. As is seen, the oxidation of the sample by ^{18}O atoms coming from O_2 molecules was important only during the first two minutes of exposure (the rate of production of $^{13}\text{C}^{18,16}\text{O}_2$ is less than 2 times the rate of consumption of $^{18,18}\text{O}_2$ and one molecule of O_2 consumed leads to the formation of two molecules of CO_2 from two molecules of CO when recombination is complete). After two minutes, *all* ^{18}O atoms provided by dissociation of $^{18,18}\text{O}_2$ molecules react with adsorbed ^{13}C to form $^{13}\text{C}^{16,18}\text{O}_2$. In consequence, only a small fraction of ^{18}O delivered by $^{18,18}\text{O}_2$ participated in the oxide growth. This fraction was estimated from GPA to be less than 5% of the total quantity of oxygen produced by $^{18,18}\text{O}_2$ dissociation. This proportion is about twice that of the fraction of O_2 in CO_2 (2 vol%).

The 9Cr sample surface was uniformly dark colored after exposure. Undoubtedly, a thicker oxide layer than the one formed in pure $^{49}\text{CO}_2$ had grown. The oxide layer was observed by FESEM (Fig. 10): a duplex oxide scale about 1.5 μm thick is seen. This oxide thickness was quite in good agreement with the measured mass gain, the oxide layer thickness suggested by GDOES profile (Fig. 11) and the consumption of oxygen atoms deduced from the gas phase composition evolution in Fig. 7.

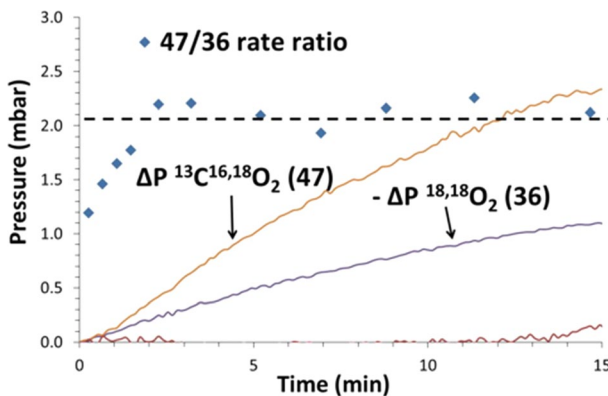


Fig. 9 Comparison between the rate of consumption of $^{18,18}\text{O}_2$ ($m/z=36$) and the rate of production of $^{13}\text{C}^{18,16}\text{O}_2$ ($m/z=47$) during corrosion test $^{49}\text{CO}_2/^{10}\text{O}_2$ for 240 min

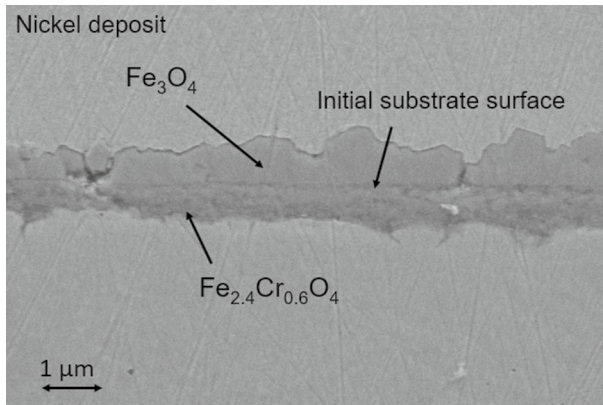


Fig. 10 FESEM image of 9Cr cross section after corrosion test $49\text{CO}_2/1\text{CO}_2$ for 240 min

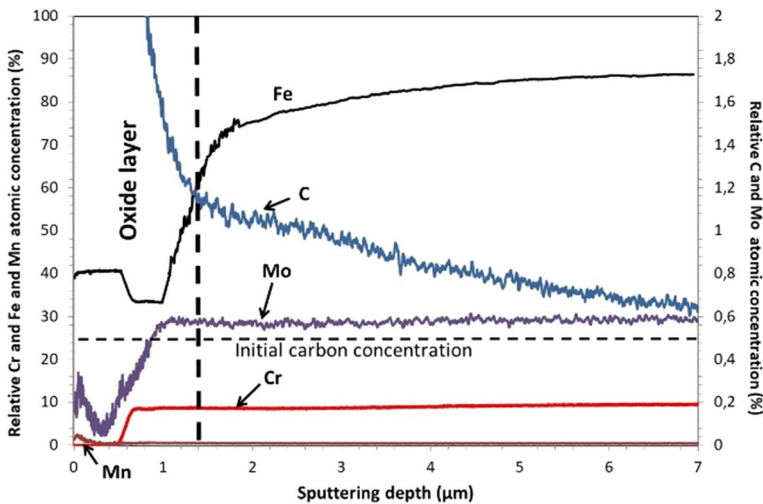


Fig. 11 Atomic fraction of Fe, Cr, Mn, Mo and C measured by GDOES through 9Cr steel surface after corrosion test $49\text{CO}_2/1\text{O}_2$ for 240 min

Using Raman Spectroscopy, the outer layer was identified as magnetite (no hematite was detected on top of it) and the inner layer as $\text{Fe}_{3-x}\text{Cr}_x\text{O}_4$. The outer/inner oxide thickness ratio was roughly equal to 1. From GDOES analysis of metal components (Fig. 11), the chromium molar fraction in the inner layer was roughly equal to that initially present in the metallic substrate, about 10 at%. In consequence, the following average stoichiometry for the inner spinel oxide scale was proposed: $\text{Fe}_{2.4}\text{Cr}_{0.6}\text{O}_4$. Moreover, no alloy chromium depletion was detected below the oxide scale.

A clear and straight interface is visible between the outer and inner oxide scale layers (Fig. 10). This interface has been shown to be the original substrate surface

in past work on corrosion of 9Cr steel in CO_2 [1, 12]. It was confirmed in this study by a complementary corrosion test on 9Cr steel with gold markers sputtered on its surface before exposure (not shown): The gold deposit was indeed detected between the outer and inner layer. Clearly, the inner oxide layer grew inwardly and the outer oxide layer grew outwardly.

Finally, the GDOES profile revealed carbon enrichment below the oxide scale. Thanks to SIMS analysis, it was possible to discriminate between carbon coming from CO_2 (^{13}C) and carbon present in the substrate initially (^{12}C). The net ^{13}C fraction is presented in Fig. 12. This net ^{13}C fraction is the ^{13}C intensity measured by SIMS minus the ^{13}C intensity induced by its presence in natural carbon (1.1 at% of total carbon intensity). ^{13}C enrichment was clearly observed below the oxide scale and into the inner part of the oxide scale at a lesser level (Fig. 12). The ^{18}O profile in the oxide scale is also shown in Fig. 13. The ^{18}O profile is quite flat through the oxide scale at a fraction of 2 at %. This level of ^{18}O is in very good agreement with the calculated level of ^{18}O transferred into the substrate from GPA.

49 CO_2 /10 $_2$ for 20 min

The morphology, structure and composition of the oxide layer formed on 9Cr steel exposed for a shorter exposure time, 20 min, was studied in more detail by TEM analyses. As shown in Fig. 14, a duplex oxide layer was formed again. However, the ratio between the outer and the inner oxide thicknesses was about 3, much higher than after 240 min (ratio=1). The 600 nm thick outer layer is seen to be compact with large columnar magnetite grains (identified by diffraction) with a few large voids near the inner layer. The 200 nm thick inner oxide layer was more complex in term of composition and microstructure: an intimate mixture of tiny $\text{Fe}_{3-x}\text{Cr}_x\text{O}_4$ and Fe_3O_4 oxide grains surrounded by nanometer sized voids (bright contrast in

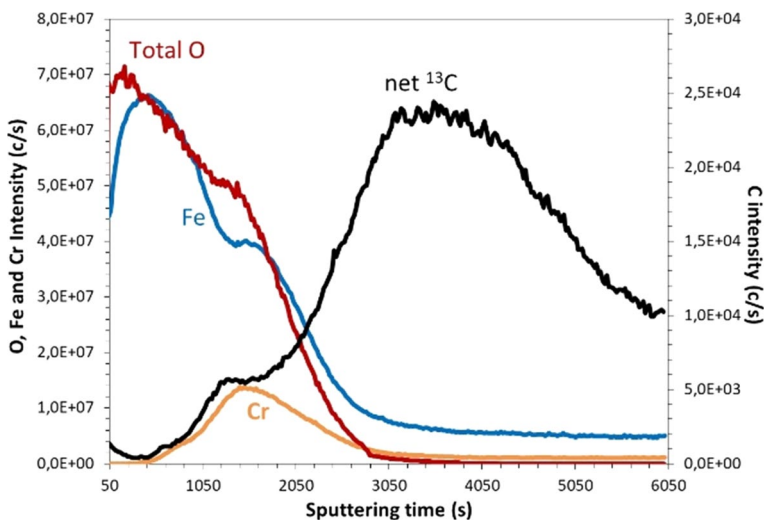


Fig. 12 SIMS profile across 9Cr surface after exposure in 49 CO_2 /10 $_2$ for 240 min

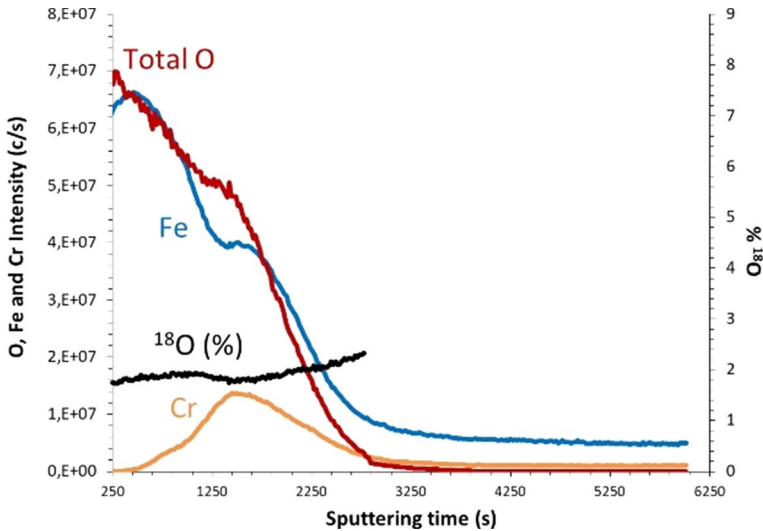


Fig. 13 SIMS measurements of ^{18}O in the oxide scale after exposure in $49\text{CO}_2/1\text{O}_2$ for 240 min. The natural isotopic abundance of ^{18}O in natural O_2 is 0.2%

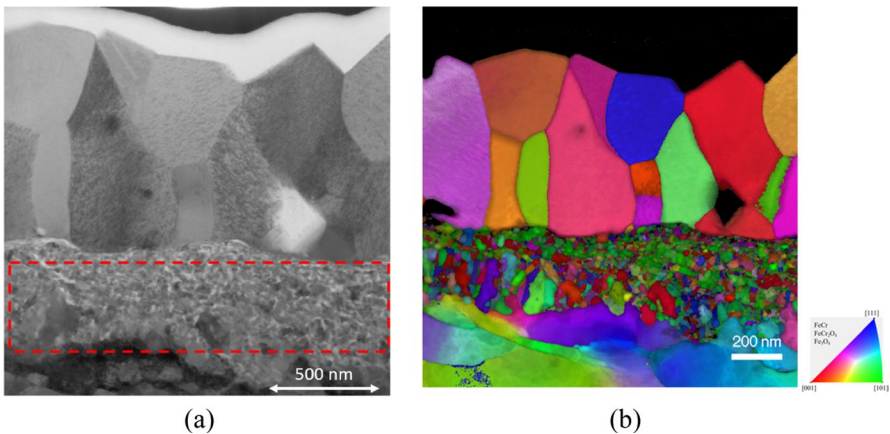


Fig. 14 **a** Bright Field STEM-image and **b** TEM-ASTAR orientations along direction perpendicular to interface metal/oxide map combined with index of the duplex oxide scale formed on 9Cr steel after exposure in $49\text{CO}_2-1\text{O}_2$ at $550\text{ }^\circ\text{C}$ for 20 min

Fig. 14a)). The composition of the oxide layer was measured by EDS-TEM. The average stoichiometry of the inner oxide scale was $\text{Fe}_{1.8}\text{Cr}_{1.2}\text{O}_4$ revealing a higher chromium molar fraction than after 240 min of exposure ($\text{Fe}_{2.4}\text{Cr}_{0.6}\text{O}_4$). The volume fraction of the tiny voids present in the inner layer was calculated from Image J software (Fig. 15) to be between 7 and 9%. No chromium depletion was detected in the substrate below the oxide scale.

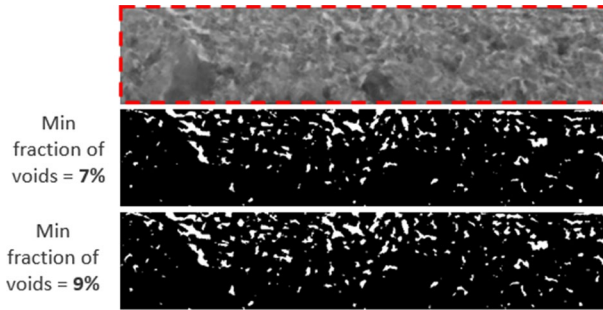


Fig. 15 Void fraction in the inner spinel oxide layer shown in Fig. 14 determined by Image Analysis by two different levels of white for criteria

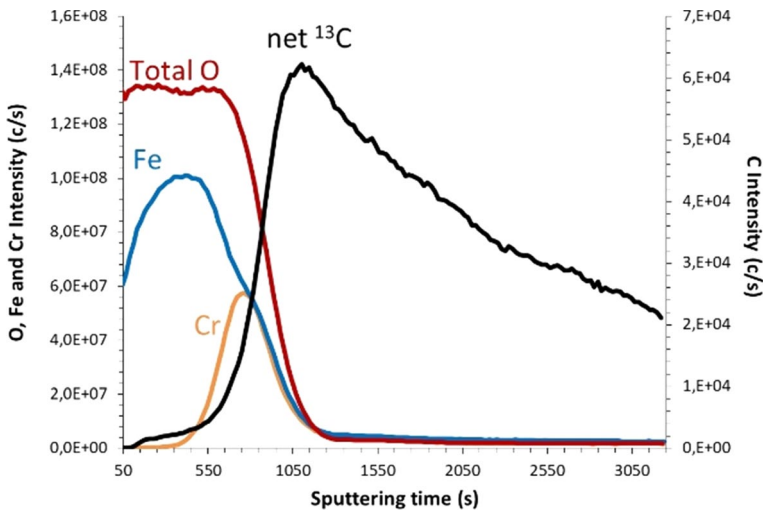


Fig. 16 SIMS profile of the oxide scale formed on 9Cr with gold deposit after exposure in $49\text{CO}_2\text{-}10\text{O}_2$ at $550\text{ }^\circ\text{C}$ for 20 min

The oxide composition and carbon enrichment from the environment (^{13}C) was determined by SIMS analysis (Fig. 16). Again ^{13}C was detected in the metallic substrate with a maximum enrichment at the metal-oxide interface. The % of ^{18}O in the oxide scale was again homogeneously distributed in the oxide scale. Its fraction was slightly higher than the one measured previously, 3% compared to 2% (Fig. 17). This result is in good agreement with the fact that the proportion of $^{18}\text{O}_2$ among all CO_2 and O_2 molecules which reacted during this 10 min exposure is slightly higher.

Corrosion in CO_2 with High Concentrations of O_2 (High $P_{\text{O}_2}/P_{\text{CO}_2}$ Ratio)

Corrosion of 9Cr steel was studied in environments containing varying fractions of O_2 : $49\text{CO}_2\text{-}5\text{O}_2$, $49\text{CO}_2\text{-}10\text{O}_2$, $49\text{CO}_2\text{-}20\text{O}_2$, and $40\text{CO}_2\text{-}40\text{O}_2$ (all partial

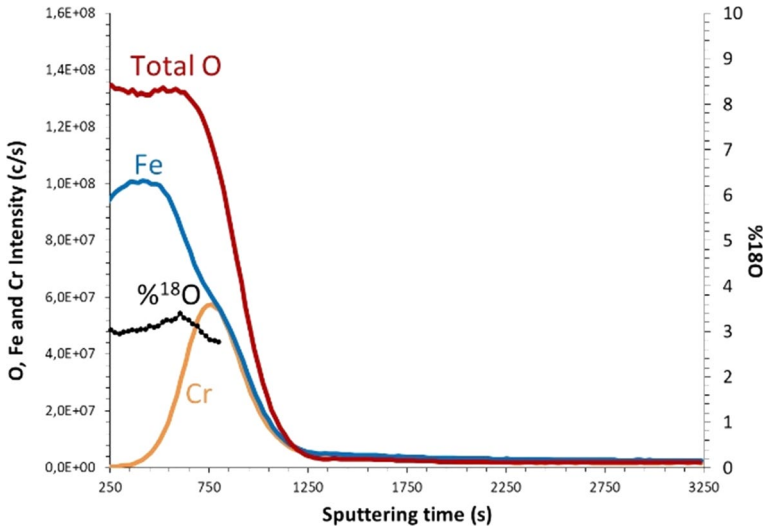


Fig. 17 ^{18}O in the oxide scale formed on 9Cr with gold deposit after exposure in $49\text{CO}_2\text{-}1\text{O}_2$ at $550\text{ }^\circ\text{C}$ for 20 min. The natural isotopic abundance of ^{18}O in natural O_2 is 0.2%

pressures in mbar). After 240 min of exposure, it was observed that the oxide scale formed in $49\text{CO}_2\text{-}5\text{O}_2$ was similar in nature and microstructure to the one formed in $49\text{CO}_2\text{-}1\text{O}_2$, but thicker. The molar consumption of oxygen atoms was quantified from GPA analysis from the following formula:

$$\text{Total } |\Delta n(\text{O})| = 2 \left| \Delta n(\text{O}_2) \right| + |\Delta n(\text{CO})|, \quad (\text{R4})$$

Where $\Delta n(\text{O}_2)$ and $\Delta n(\text{CO})$, the molar quantity of consumed O_2 and produced CO molecules are calculated from the pressure evolution. The final consumption of oxygen was higher after reaction in 5 mbar than in 1 mbar O_2 (Fig. 18). However, a closer examination of the oxidation kinetics showed that the oxidation rate within the first fifteen min of exposure was quite similar for both gases. The main difference was that the oxidation rate did not decrease significantly after fifteen minutes in $49\text{CO}_2\text{-}5\text{O}_2$. This observation can be linked to the continued presence of O_2 molecules in the reaction chamber for a longer period, resulting in a delay in the formation of CO molecules (by oxidizing adsorbed CO to CO_2 molecules) and continued metal oxidation (Fig. 19).

Interestingly, at higher pressure than 5 mbar of O_2 in CO_2 , the final measured mass gain after reaction for 20 min started to decrease, and the amplitude of this decrease increased with the O_2 proportion (see Fig. 20). At these higher pressures of O_2 in CO_2 , 9Cr steel surface was covered both by thick and thin oxide scale as described in Sect. 3d. The lower the mass gain, the higher the proportion of thin scale on the surface. The thin scale was still duplex, but the outer part was made of hematite instead of magnetite. Much less ^{13}C was transferred when thin oxide scale was formed (compare Figs. 12 and 21). The mass gain of 9Cr sample exposed in

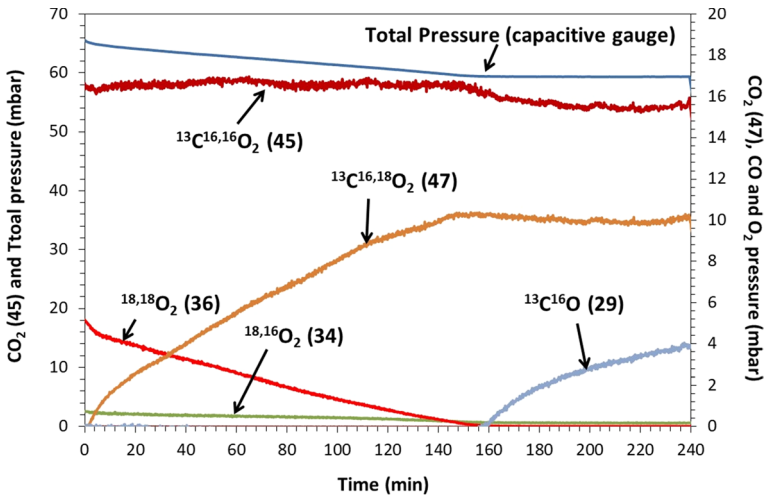


Fig. 18 Gas phase composition measured by MS during corrosion test in 49CO₂-5O₂ at 550 °C for 240 min

the binary 40O₂-40CO₂ environment was only 1.5 times higher than the mass gain observed in 15 mbar of pure O₂ (Fig. 20). Both samples were covered by thick and thin oxide scale with the proportion of thick oxide scale slightly higher for the sample exposed in 40CO₂-40O₂.

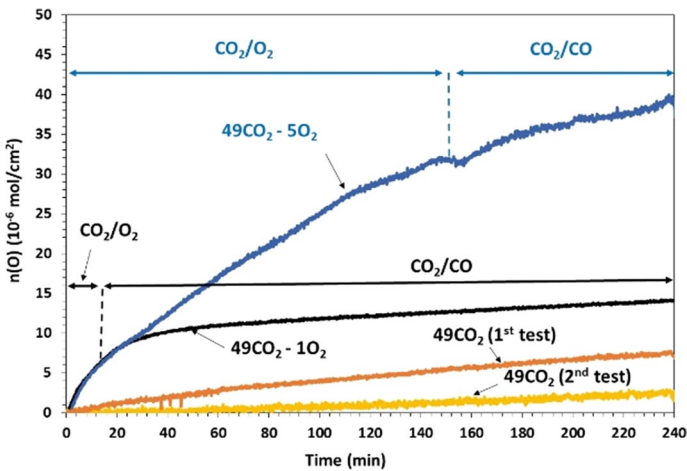


Fig. 19 Oxidation kinetics of 9Cr steel in 49CO₂, 49CO₂-1O₂ and in 49CO₂-5O₂ at 550 °C for 240 min. Two test were carried out in 49CO₂. 10⁻⁶ mol of O/cm² corresponds to a 110 nm thick equivalent Fe₂O₃ oxide scale

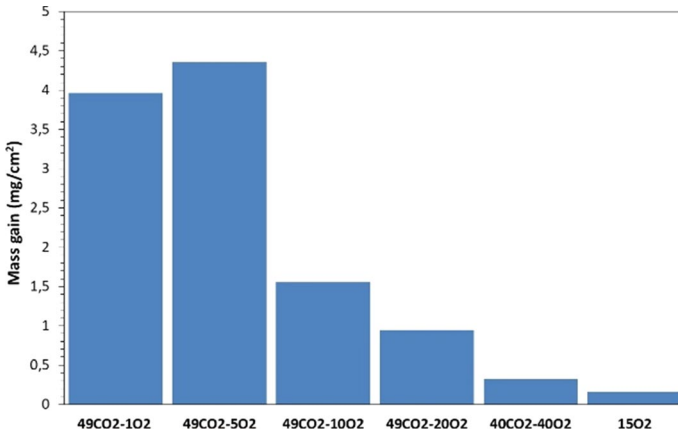


Fig. 20 Mass gain of 9Cr sample after 20 min of exposure in various CO₂/O₂ gas composition (mbar)

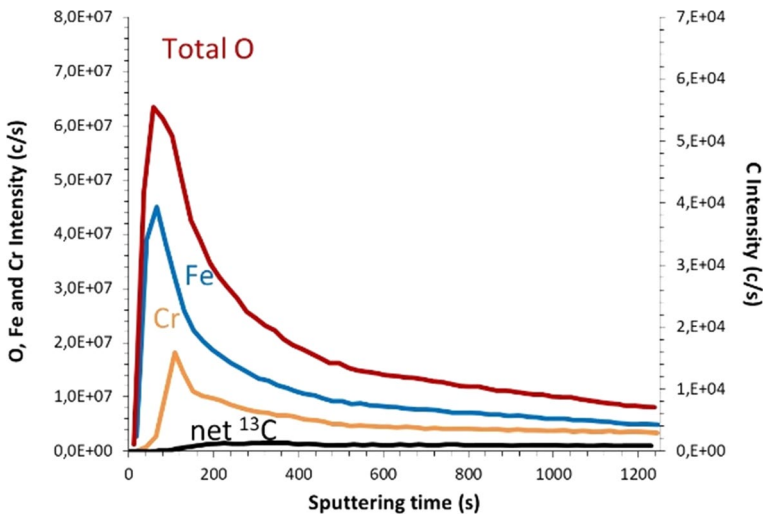


Fig. 21 SIMS profile of the oxide scale formed on 9Cr after exposure in 49CO₂-200O₂ at 550 °C for 20 min

Corrosion in Pure O₂

A 9Cr sample was exposed in 1 mbar O₂ at 550 °C for 20 min. Reaction kinetics are revealed by the gas phase analysis shown in Fig. 22. Consumption of O₂ and production of CO₂ were observed revealing oxidation of the carbon contained in the sample. After 20 min, about 0.7 mbar of the 1 mbar of O₂ initially present at room temperature had reacted. Only 0.3 mbar of CO₂ had been produced, demonstrating that metal oxidation occurred as well. The reaction rate of O₂ molecules

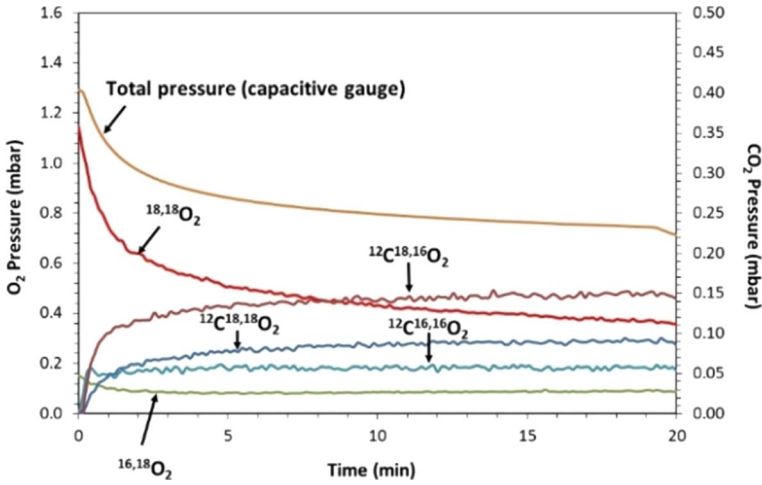


Fig. 22 Evolution of the gas phase composition measured by MS during the exposure of 9Cr steel in $1O_2$ at 550 °C for 20 min

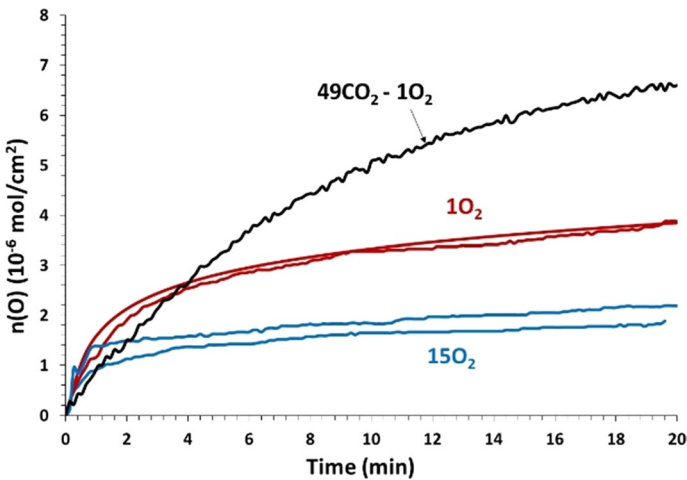


Fig. 23 Comparison of the oxidation kinetics of 9Cr steel in $49CO_2-1O_2$ and in pure O_2 (1 and 15 mbar). 10^{-6} mol of O/cm^2 corresponds to a 110 nm thick equivalent Fe_2O_3 oxide scale

was high within the first minute, but then decreased drastically as did the production of CO_2 . Thus, both the oxide scale growth rate and the decarburization rate decreased after one minute. The oxidation kinetics of 9Cr steel in pure O_2 and in CO_2/O_2 mixtures are compared in Fig. 23. The oxidation rate in $1O_2$ was much higher than in $49CO_2-1O_2$ within the first minutes. But then, it decreased drastically in $1O_2$, whereas the oxidation rate in $49CO_2-1O_2$ was still high.

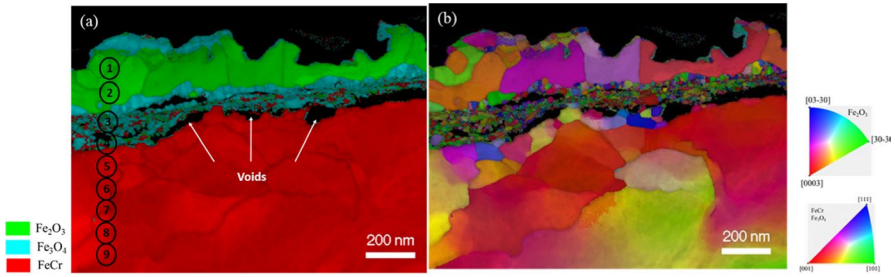


Fig. 24 **a** TEM-ASTAR phase map combined with index (green = hematite; blue = magnetite; red = substrate) and **b** TEM-ASTAR orientations (along direction perpendicular to metal/oxide interface) map combined with index of the oxide layer formed on 9Cr in zone A after exposure in 1O_2 for 20 min (Color figure online)

Table 3 Fe and Cr composition (in at %) determined by TEM-EDS on Fig. 24 (a) (“thick oxide scale”, one A)

Analyzed area	Outer oxide layer		Inner oxide layer		Metallic substrate				
	1 and 2		3	4	5	6	7	8	9
Fe (at %)	> 99		39	30	91	90	90	90	90
Cr (at %)	< 1		61	70	10	10	11	11	11

Increasing the pressure of O_2 from 1 to 15 mbar decreased the mass gain after 20 min (Fig. 23). The oxidation rate was slightly lower after 30 s but decreased drastically hereafter.

The oxide layer formed on 9Cr steel surface after exposure in 1O_2 for 20 min was observed by TEM. The oxide scale was quite heterogeneous in thickness and microstructure. Two different zones were clearly identified: zone A, about 200–500 nm thick oxide described here as “thick oxide scale” and zone B, about 50–100 nm thick oxide described as “thin oxide scale”.

The “thick oxide scale” (zone A) is shown in detail in Fig. 24. The morphology and microstructure of this oxide layer were very similar to the oxide layer formed in $49\text{CO}_2-1\text{O}_2$ (Fig. 14). The composition was also similar: The outer scale was iron oxide only, the inner scale was a mixture of iron and chromium oxide and no chromium depletion was evidenced below the scale (Table 3). However, there exists a major difference: The outer oxide scale was hematite and not magnetite. The presence of hematite at the gas–oxide interface was confirmed by Raman spectroscopy (not shown) and by XPS analysis (not shown) where only Fe^{3+} could be detected. Moreover, the inner Fe–Cr spinel oxide layer was richer in chromium than the one formed in $49\text{CO}_2-1\text{O}_2$, with an average stoichiometry approximating to FeCr_2O_4 from TEM–EDX analyses given in Table 3. No chromium depletion was detected in the substrate below the chromium-rich scale from Fig. 24 and Table 3. Finally, this “thick oxide scale” was thinner than the one formed in $49\text{CO}_2-1\text{O}_2$.

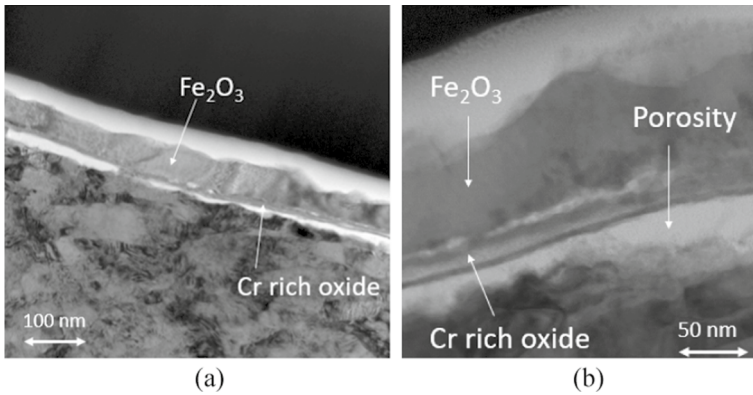


Fig. 25 Bright Field-STEM image of zone B (“thin oxide scale”) at two different scales

STEM images of the “thin oxide scale” (zone B) are shown in Fig. 25 where a duplex oxide scale is clearly visible. The outer layer is again made of hematite, with chromium-rich oxide formed below it. An almost continuous gap was observed below the chromium-rich oxide separating physically the oxide scale from the metallic substrate.

The proportion of “thin oxide scale” (zone B) was higher on sample exposed to higher P_{O_2} (15 mbar). This observation is in agreement with the lower oxidation kinetics shown in Fig. 23.

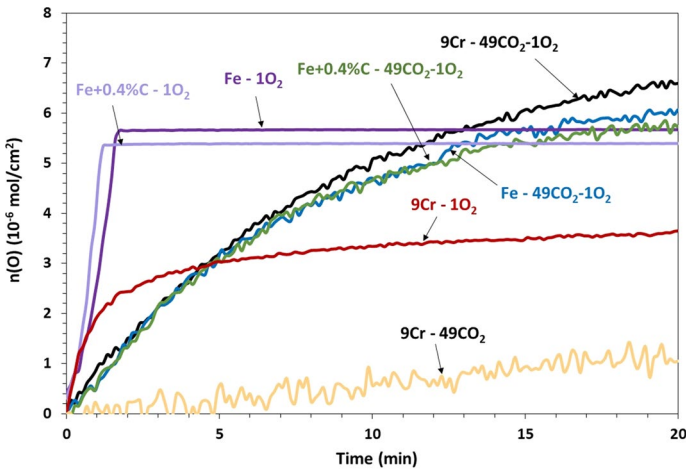


Fig. 26 Oxidation kinetics (measured by the total quantity of oxygen moles consumed as a function of time) within the first 20 min of exposure for iron, mild steel and 9Cr steel exposed in $49CO_2-1O_2$, $49CO_2$ and $1O_2$ at 550 °C. 10^{-6} mol of O/cm^2 corresponds to a 110 nm thick equivalent Fe_2O_3 oxide scale

Comparison of the Oxidation Kinetics of 9Cr, Iron and Mild Steel in O_2 and CO_2-O_2

Figure 26 compares the oxidation kinetics of iron, mild steel, and 9Cr steel when exposed to O_2 , CO_2-O_2 gas mixtures, and $He-O_2$ at 550 °C for a duration of 20 min. The results obtained for iron and mild steel were extracted from [10].

Interestingly, the oxidation rates of iron, mild steel, and 9Cr steel in $1O_2$ were equal for the first 30 s, reaching approximately $2.8 \mu\text{mol}/\text{cm}^2/\text{min}$ equivalent to 300 nm/min (if considering Fe_2O_3 growth). However, after this initial period, the oxidation kinetics diverged significantly between iron/mild steel on one side and 9Cr steel on the other side. The oxidation rate of 9Cr steel experienced a drastic decrease, and only half of the O_2 molecules in the reactor were consumed after 20 min, resulting in an oxide thickness of about 400 nm. This led to the formation of a duplex oxide scale with hematite in the outer part and voids at the oxide/metal interface as detailed previously. In the case of iron and mild steel, all O_2 molecules were consumed within the first two minutes of exposure, resulting in an oxide scale thickness of around 650 nm. Only magnetite was detected, and the scale remained well attached to the substrate.

In $49CO_2-1O_2$, the observed oxidation kinetics over the 20-min exposure period were similar for all three materials. The oxidation rate was approximately 80 nm/min for the first two minutes which is about four times lower than in $1O_2$ and gradually decreased after longer times. After 20 min, the three materials reached a final oxide thickness of approximately 600–700 nm. This result demonstrates that the presence of Cr had no effect at all on the oxidation rate of the alloy in $49CO_2-1O_2$ which differs strongly from what has been observed previously in pure O_2 .

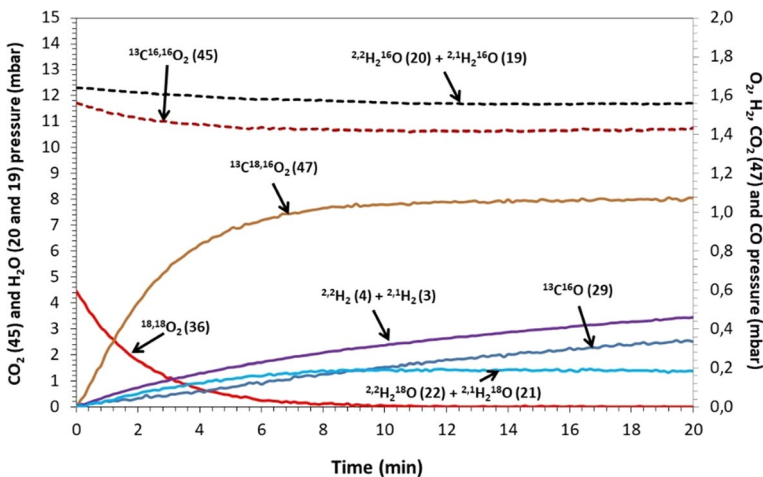


Fig. 27 Gas phase composition measured by MS during corrosion test in $10CO_2-1O_2-10^2H_2O$ at 550 °C for 20 min

Influence of H₂O in CO₂/O₂

The influence of water vapour on the corrosion behaviour of “as received” 9Cr foil sample was evaluated through exposure tests at 550 °C for 20 min in 10CO₂-0.5O₂-x²H₂O gas mixtures with increasing x values, typically 1, 5 or 10 mbar. The GPA results for the tests in 10CO₂-0.5O₂-10²H₂O are shown in Figs. 27.

As is seen in Fig. 27, the reactivity of a Cr steel in 10CO₂-0.5O₂-10²H₂O is quite similar to CO₂-O₂. Both ^{18,18}O₂ (*m/z*=36), ¹³C^{16,16}O₂ (*m/z*=45) and ²H₂¹⁶O (*m/z*=20 and 19) molecules dissociated on the surface to form ¹⁸O, ¹⁶O atoms and ¹³CO and ²H₂ molecules. Almost all ¹⁸O atoms reacted with CO and H₂ to form CO₂ (*m/z*=47) and H₂O (*m/z*=21 and 22) again. The proportion of ¹⁸O atoms forming CO₂ molecules was higher than that forming H₂O (85% and 15% respectively). CO (*m/z*=29) and H₂ (*m/z*=3 and 4) molecules were also formed. As observed in CO₂-O₂ gas mixtures, the proportion of released CO was much lower than CO₂ (*m/z*=47) when O₂ was present in the reactor. This was not the case for H₂ (*m/z*=3 and 4) and H₂O (*m/z*=21 and 22) which were formed at almost the same rate. When O₂ was consumed totally in the reactor, only CO (*m/z*=29) and H₂ (*m/z*=3 and 4) were produced.

9Cr steel formed a similar duplex oxide scale in structure such as shown in Fig. 10 in all 10CO₂-0.5O₂-x²H₂O gas mixtures. The mass gain increased with increasing the partial pressure of x²H₂O in the gas mixture. The mass gain was about 30% higher in 10CO₂-0.5O₂-10²H₂O compared to 10CO₂-0.5O₂-1²H₂O. The oxide thickness of the duplex oxide scale formed 10CO₂-0.5O₂-x²H₂O gas mixtures for 20 min was between 0.6 and 0.8 μm.

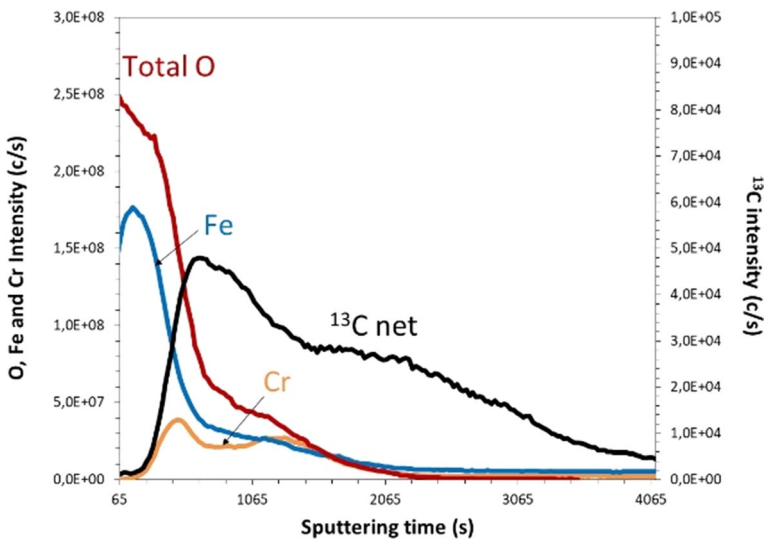


Fig. 28 SIMS profile of the oxide scale formed on 9Cr after exposure in 10CO₂-0.5O₂ for 20 min

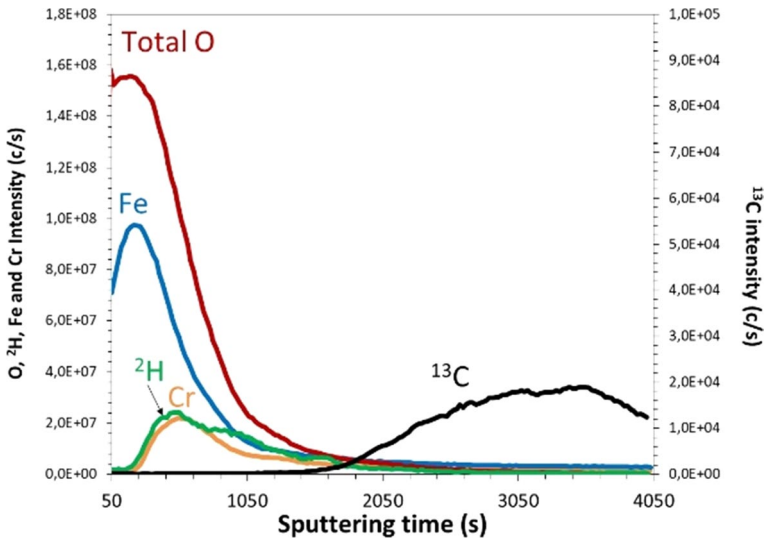


Fig. 29 SIMS profile of the oxide scale formed on 9Cr after exposure in $10\text{CO}_2-0.5\text{O}_2-1^2\text{H}_2\text{O}$ for 20 min. ^2H intensity was multiplied by 10^4

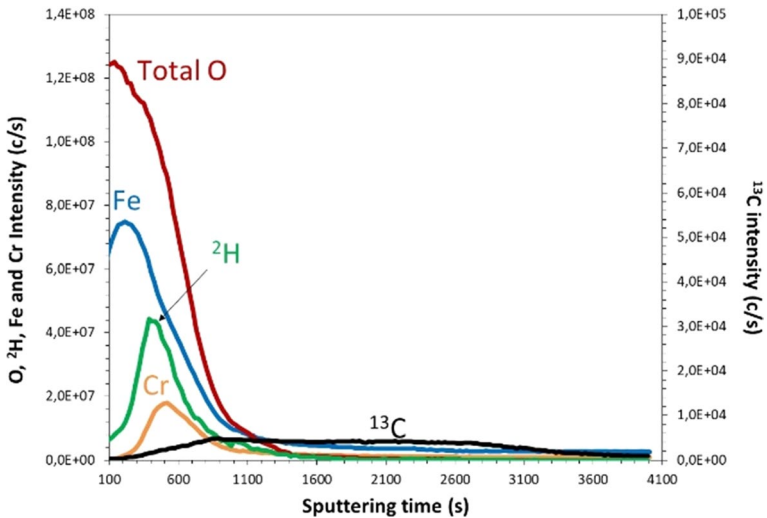


Fig. 30 SIMS profile of the oxide scale formed on 9Cr after exposure in $10\text{CO}_2-0.5\text{O}_2-5^2\text{H}_2\text{O}$ for 20 min. ^2H intensity was multiplied by 10^4

Scale composition measured by SIMS with a particular focus on the incorporation of ^{13}C and ^2H , are shown in Figs. 28, 29, 30, and 31 for samples oxidized for 20 min in the various $10\text{CO}_2-0.5\text{O}_2-x^2\text{H}_2\text{O}$ gas mixtures. Only duplex oxide scale with the structure shown in Fig. 14 formed on the samples exposed in H_2O containing CO_2/O_2 gas mixtures. A small fraction of the 9Cr surface exposed in $10\text{CO}_2-0.5\text{O}_2$

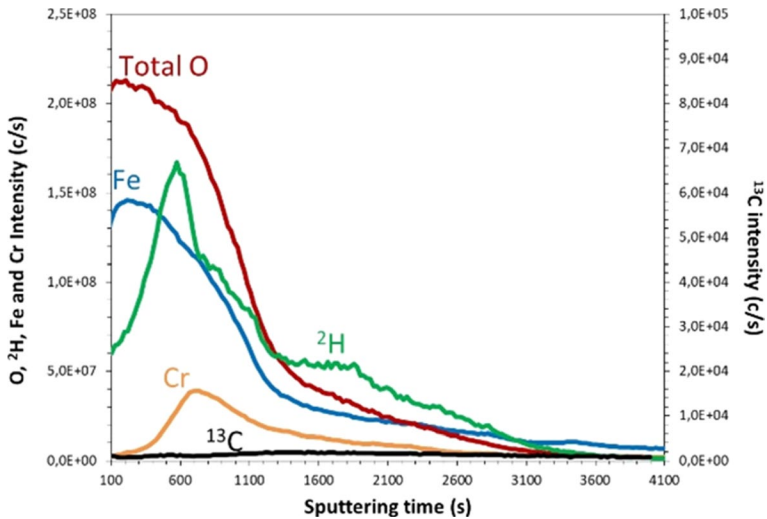


Fig. 31 SIMS profile of the oxide scale formed on 9Cr after exposure in $10\text{CO}_2\text{-}0.5\text{O}_2\text{-}10^2\text{H}_2\text{O}$ for 20 min. ^2H intensity was multiplied by 10^4

was covered by thin oxide scale (as in Fig. 25), the other part being covered by thick oxide scale which explains why two chromium peaks were observed in Fig. 28 (uneven surface).

For the sample exposed in $10\text{CO}_2\text{-}1\text{O}_2$, high amount of ^{13}C was detected in the inner oxide layer and in the metallic substrate below (Fig. 28) as for the sample exposed in $49\text{CO}_2\text{-}1\text{O}_2$ (Fig. 16). The amount of ^{13}C transferred into the substrate decreased with the increase of $^2\text{H}_2\text{O}$ pressure. Almost no carbon transfer occurred in $10\text{CO}_2\text{-}0.5\text{O}_2\text{-}10^2\text{H}_2\text{O}$. Moreover, ^2H enrichment was clearly detected into the inner oxide layer, where chromium was present. Interestingly, the ^2H profile was quite similar to the Cr profile. Almost no ^2H was detected in the outer magnetite layer. The amount of H in the oxide scale increased with the increase of $P_{\text{H}_2\text{O}}/P_{\text{O}_2}$ ratio. In a total pressure of 21 mbar, carburization was completely suppressed at a $\text{H}_2\text{O}/\text{CO}_2$ ratio equal to 1.

Discussion

Preliminary Remarks

A complex pattern of behavior by the 9Cr1Mo ferritic-martensitic steel during oxidation in different gases at $550\text{ }^\circ\text{C}$ has been revealed. The discussion commences with an examination of the Fe–Cr–O gas–solid thermodynamics, which reveals that many of the reactions do not achieve local equilibrium and are instead kinetically controlled. A brief summary of reaction product morphologies is then used to relate oxidation rates to the extent of chromium enrichment in the scales. This is of importance to the different degrees of protection offered by the

Table 4 Description of the corrosion behavior of 9Cr foil as a function of gas composition, H = Hematite; S = Spinel; M = Magnetite; C = Corundum

Gas, exposure time	Scale morphology and phases	Oxide thickness	Scale Cr content [Cr]/[Cr]+[Fe]	Feature	Carburization
1 mbar O ₂ , 20 min	Thick duplex oxide scale (Outer = H ; Inner = S) + Thin duplex oxide scale (Outer = H ; Inner = C)	Thin : 50–100 nm Thick : 200–500 nm	Thin : Inner > 95 % Inner ≈ 70 %	Presence of large voids at the oxide metal/interface	–
15 mbar O ₂ , 20 min	Thick duplex oxide scale (Outer = H ; Inner = S) + Thin duplex oxide scale (Outer = H ; Inner = C)	Thin : 50–100 nm Thick : 200–500 nm	Thin : Inner > 95 % Inner ≈ 70 %	Proportion of the surface covered by the thin duplex oxide scale twice of that observed in 1 mbar	–
1 mbar CO ₂ , 4 h	Single oxide scale, C	50 nm	≈ 80 %	–	Very Low
49 mbar CO ₂ , 4 h	Single oxide scale, C	250 nm	≈ 50 %	–	Very Low
49 mbar CO ₂ + 1 mbar O ₂ , 20 min	Duplex oxide scale Outer = M ; Inner = S	600 nm	Inner : ≈ 67 %	Porous inner spinel layer structure	High
49 mbar CO ₂ + 1 mbar O ₂ , 4 h	Duplex oxide scale Outer = M ; Inner = S	1.5 μm	Inner : ≈ 43 %	Porous inner spinel layer structure	High
49 mbar CO ₂ + x mbar O ₂ , 20 min	Thick duplex oxide scale (Outer = M ; Inner = S) + Thin duplex oxide scale (Outer = H ; Inner = C)	Between 200 and 600 nm	Thin : Inner > 95 % Inner ≈ 43 %	The proportion of the surface covered by the thin duplex oxide scale increased with O ₂ /CO ₂ ratio	Decrease with the P _{O₂} /P _{CO₂} ratio
10 mbar CO ₂ + 1 mbar O ₂ , 240 min	Thick duplex oxide scale (Outer = M ; Inner = S) + Thin duplex oxide scale (Outer = H ; Inner = C)	Thick : ≈ 600 nm	Thin : Inner > 95 % Inner ≈ 43 %	/	High
10 mbar H ₂ O + 1 mbar O ₂ , 240 min	Thick duplex oxide scale (Outer = M ; Inner = S)	≈ 800 nm	Inner : ≈ 43 %	Presence of H in the inner oxide scale	–
49 mbar CO ₂ + 1 mbar O ₂ + x mbar H ₂ O, 20 min	Thick duplex oxide scale (Outer = M ; Inner = S)	between 600 and 800 nm	Inner : ≈ 43 %	Presence of H in the inner oxide scale	Decrease with the P _{H₂O} /P _{CO₂} ratio

various scales, and possible means of achieving better alloy performance. Gas phase analysis results are used in conjunction with high resolution analyses of the corrosion reaction products to identify detailed chemical processes involved in the gas–scale interactions. An oxidation scenario is proposed for all gas mixtures (pure CO₂, CO₂ with low and high pressure of O₂ and pure O₂). Finally, the influence of H₂O on the corrosion behavior in CO₂–O₂ gas mixtures is examined.

Thermodynamics, Reaction Products and Kinetics

The various results reported here are summarized in Table 4. It shows that the corrosion behavior of 9Cr steel in CO₂/O₂ environments at 550 °C was strongly dependent on the CO₂/O₂ ratio in the environment. As it will be demonstrated, the corrosion behavior and kinetics are strongly dependent on the oxidizing potential imposed at the gas–oxide surface at any time and, more importantly, within the first instants of reaction since its value strongly influences the nature, morphology and microstructure of the resulting oxide scale. From a thermodynamic point of view, the CO₂, H₂O, O₂ or CO₂/O₂/H₂O gas mixtures used here can all form iron and chromium oxide and oxidize carbon (Fig. 32). Nevertheless, very different corrosion behavior patterns were observed as a function of the gas phase composition and total gas pressure. In that sense, thermodynamic prediction of which oxide should form is of limited use here, and the effect of the other chemical species, carbon and oxygen, must be taken into account.

The details of solid–gas interaction are important as they determine which phases and microstructures form on the steel surface. This leads to substantial differences in behavior of 9Cr steel in different gases.

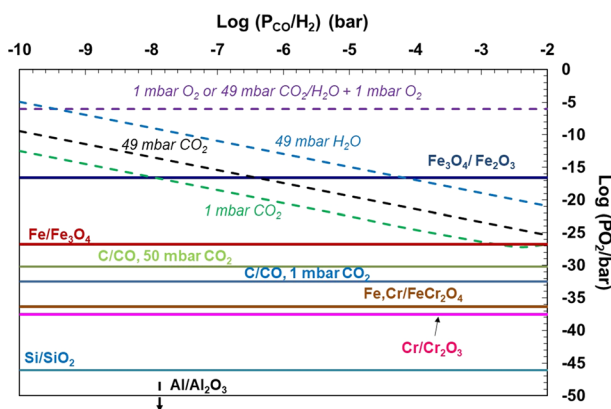


Fig. 32 Equilibrium oxygen partial pressure imposed by a CO₂/CO gas mixture as function of CO pressure (or H₂ pressure when considering H₂O) compared to the equilibrium oxygen partial pressure for the main metallic elements of 9Cr steel at 550 °C. The activities of all metallic elements were taken equal to their atomic fractions in 9Cr steel. The activity of carbon was taken equal to 10⁻⁶ (from Thermocalc)

Corrosion Behavior of 9Cr Steel in Pure CO₂

When exposed to pure CO₂, the steel formed a slow growing thin “single” Fe/Cr-rich oxide scale (Fig. 2). This oxide scale formation was accompanied by a small amount of transient decarburization of ¹²C initially present in the steel and a very slight injection of ¹³C from the gas phase. Decarburization in pure CO₂ is in good agreement with previous observations made on iron and mild steel in pure CO₂ [10]. Nevertheless, for 9Cr steel, decarburization is very slight and appears to be transient which was not the case for iron/mild steel. The reason for this difference lies in the fact that 9Cr forms an oxide scale, whereas iron and mild steel formed no oxide. Moreover, it was observed that the Cr/(Fe + Cr) ratio in the oxide scale increases with the decrease of P_{CO₂} (50 at% in 49 mbar against 80 at% in 1 mbar). At the lowest CO₂ pressure, 1 mbar, the most stable oxide forming elements, Al and Si, which are minority components of 9Cr steel are present in the oxide scale in great quantity compared to their very low concentrations initially in the substrate. These observations cannot be understood from a thermodynamic point of view alone, since the oxidation of the major elements, Fe, C, Cr and minor elements Mn, Al and Si are always possible, whatever the gas phase P_{CO₂} value (Fig. 32).

These observations demonstrate that the surface reaction and composition of the oxide scale are governed by the rate of surface reaction of CO₂, a conclusion already reached [10] for reaction of CO₂ with iron and mild steel. The rate of dissociation of CO₂ is low and, in consequence, the availability of oxygen atoms free to react with the surface is strongly linked to the p(CO₂) value. The oxygen atoms produced by CO₂ dissociation react in the very initial stage with all surface metal atoms capable of forming stable oxides. The resulting mix of iron and chromium oxides can be kinetically unstable with respect to the underlying alloy. If oxidation is slow compared with alloy diffusion, Cr can diffuse to the alloy surface, there to reduce iron oxide yielding Cr-rich oxide.

In low CO₂ pressure gas, the number of O atoms produced is very low and the most stable oxide forming elements have time to diffuse from the metallic substrate to reach the surface and react when new O atoms are produced on the surface. Such a scenario explains why Al- and Si-enriched oxide scale is preferentially formed in low P_{CO₂} (1 mbar), and why the chromium enrichment in the scale is increased by decreasing P_{CO₂} from 49 to 1 mbar. There is a clear link between the rate of oxidation during the initial instant of exposure and the level of chromium enrichment in the oxide scale. In higher CO₂ pressure (here 49 mbar), the number of dissociatively adsorbed O atoms increases. In this situation, iron starts to oxidize since the diffusion rates of Al and Si are not fast enough to reach the surface and react with and reduce the Fe-rich oxide. The higher concentration of Cr in the steel also permits its enrichment in the scale, but not to the same degree as in the slower growing scale formed in 1 mbar CO₂.

For 9Cr steel, decarburization appeared to slow down after the formation of the oxide layer on the surface which differed, again, from mild steel exposed in pure CO₂. Two reasons could explain this observation: either the chromium-rich oxide layer formed on 9Cr steel is more gas-tight than the iron oxide layer formed on iron and mild steel and/or the activity of carbon reached below the oxide layer is so low

that the decarburization rate becomes negligible. The first assumption is very likely as Cr_2O_3 has been demonstrated to be impermeable to carbon diffusion [13].

Corrosion Behavior in CO_2 Plus Low Pressure O_2

Acceleration of Initial Oxidation Rate

When O_2 was added to CO_2 , the corrosion behavior of 9Cr steel was drastically altered. The steel formed a fast growing, iron-rich duplex oxide scale while undergoing strong internal carburization. This corrosion behavior is the one usually observed by 9-12Cr steel in atmospheric or high-pressure industrial grade CO_2 at temperatures below 600 °C [1, 4, 9, 12, 15]. As evidenced by Fig. 26, the oxidation rate of the duplex oxide layer formed in 49 mbar CO_2 with 1 mbar O_2 was high within the first minutes of exposure when O_2 was still present in the reactor, about one order of magnitude higher than in pure CO_2 . Significantly, this fast initial oxidation rate was not influenced by the presence of chromium, since roughly the same oxidation rate was observed for iron and mild steel in the same environment (Fig. 26). The strong corrosion behavior difference between reaction with pure CO_2 and CO_2 with 1 mbar O_2 can be explained by a surface reaction limited oxidation process during the first instants of exposure.

The following scenario of oxide formation and growth is proposed. During exposure of 9Cr steel, the O_2 and CO_2 molecules contained in the gas phase adsorb on the surface, dissociate and the generated atoms (O) or molecules (CO) react again with each other and/or with the alloying elements (metallic elements and/or carbon). The number of adsorbed O atoms available at any time to form oxide depends on many successive processes: the impingement rates of CO_2 and O_2 molecules, their dissociative adsorption rate to form O atoms on the surface, the rates of reaction of O atoms with other adsorbed molecules or atoms on the surface (such as CO molecules) and the rate of incorporation into an oxide unit cell. All these events have been detailed in a previous study for exposure of iron and mild steel in CO_2 - O_2 gas mixtures at 550 °C [10]. In that study [10], it was demonstrated that the oxidation rate of iron was initially controlled almost exclusively by the dissociation rate of adsorbed O_2 , and that adsorbed CO_2 acted mainly by limiting O_2 access to the surface, since its dissociation rate was much lower. For iron and mild steel, this oxidation regime where the dissociation rate of O_2 was the rate limiting step for oxide scale formation was in effect until a 1.2 μm thick iron oxide was built, whereupon the limiting step of the oxidation rate became outwards iron diffusion through the scale.

The similar oxidation rates of iron/mild steel and 9Cr steel during the first minutes of exposure suggests that the same process occurs, that is to say that the initial oxidation growth is controlled by the dissociation of O_2 molecules and that the diffusion properties of the formed oxide scale did not differ strongly between the one formed on iron and mild steel and the one formed on 9Cr steel. Since the dissociation rate of O_2 is much higher than that of CO_2 , the oxidation rate of the surface

is far higher than in pure CO_2 [10]. Thus, the presence of O_2 impurities in CO_2 increases drastically the initial oxidation rate of 9Cr steel.

As seen from Fig. 32, the equilibrium partial pressure of $49\text{CO}_2-1\text{O}_2$ is far above that needed to stabilize iron and chromium oxides. Thus, the questions of interest is how the very fast initial oxidation rate of the steel by O_2 molecules in CO_2 impacts so much the Cr enrichment of the oxide scale, its morphology and its permeability for carbon? To try to answer to these questions, an oxide growth mechanism involving several steps is proposed below.

Proposed Oxidation Mechanism for the Formation of Non-protective Fast Growing Oxide Scale on 9Cr Steel Exposed to CO_2 - O_2 Gas Mixtures

During the first instants of exposure at high temperature, the description of transient oxidation and the subsequent microstructural evolution is similar to that given for reaction in pure CO_2 (Sect. 4c). Initial reaction causes oxidation of all surface metal atoms. If the resulting structure grows slowly, Cr from the substrate has time to diffuse to the surface and reduce Fe oxide, forming Cr-rich oxide and metallic Fe. However, if transient oxidation is more rapid, the degree of Cr-enrichment achieved is less.

The concentration of adsorbed oxygen atoms increases with the value of $p(\text{O}_2)$ in the gas mixture. If the free O atom formation rate on the surface is lower or equal to the diffusion flux of metallic chromium from the alloy to its surface, chromium oxide accumulates on the surface and protective corrosion performance is achieved. This is what is observed in pure CO_2 , the dissociation of which yields the slow generation of free O atoms. If the supply of free O atoms at the surface is much higher than the flux of metallic chromium coming to the surface to react, then iron oxidize massively and iron oxide Fe_3O_4 builds on the surface. As Fe_3O_4 is known to grow fast outwardly, a large concentration of iron vacancies are created in the metallic substrate below the oxide layer [16–20]. If the substrate cannot annihilate fast enough this creation of iron vacancies, the critical iron vacancy concentration to form voids is reached and voids form ultimately. Then, oxide forms in this “available volume” by penetration of the oxidizing molecules (O_2 and CO_2) according to the so-called Available Space Model (ASM) [16, 18–20] re-named recently “Void-induced duplex oxide growth” [1, 12, 14].

In that model, the oxide grows both outwardly by reaction with the oxidizing gas phase at the gas–oxide interface and inwardly by reaction of the oxygen-depleted gas phase with metallic iron and chromium to form oxide inside the available space created by the formation of voids. Consequently, chromium atoms are “in-situ” oxidized (its outwards diffusion is too low) and the outer-inner oxide interface corresponds to the initial 9Cr steel surface. Oxidation of the metals at the oxide-steel interface by CO_2 molecules induces carburization of the substrate through the generation of CO molecules which then react through the following Boudouard reaction as already proposed in the literature [1, 15, 21–23]:

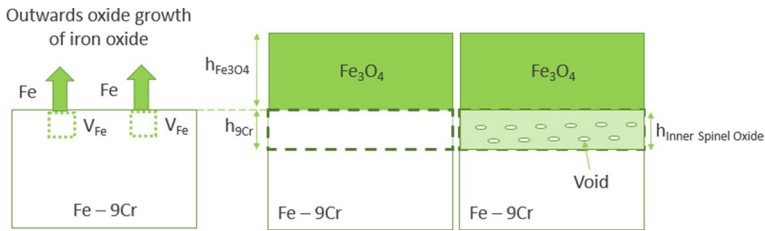


Fig. 33 Schematic of the “Available Space Model” for oxide growth



It is then proposed that the filling of voids by oxide is possible as long as pathways for fast access of the oxidizing molecules (CO_2 and O_2) into voids are available. The remnant porosity is maintained in the inner oxide layer, as observed in Figs. 14 and 15. This oxidation mechanism was first proposed by Gibbs for mild steel in dry CO_2 [16]. From quantified characteristics of the duplex scale observed by TEM (oxide thickness of the outer and inner oxide scale, %Cr in the inner layer and void fraction), calculations were carried out to verify if the duplex oxide scale formed in $49\text{CO}_2\text{-}1\text{O}_2$ and observed in Fig. 14 grows according to the “Available Space Model”. A schematic of the oxidation process is shown in Fig. 33.

To that purpose, mass balance was carried out on Fe (Eq. E1) and Cr (Eq. E2). It was assumed that the interface between the outer and the inner oxide scale corresponds to the initial substrate surface (Fig. 33). Moreover, it was assumed that the voids contain neither Fe nor Cr atoms. From these assumptions, the following expressions were obtained:

$$C_{\text{Fe}}(9\text{Cr}) * V(9\text{Cr}) = C_{\text{Fe}}(\text{Inner Spinel Oxide}) * [V(\text{Inner Spinel Oxide}) - V(\text{void})] + C_{\text{Fe}}(\text{Fe}_3\text{O}_4) * V(\text{Fe}_3\text{O}_4) \tag{E1}$$

$$C_{\text{Cr}}(9\text{Cr}) * V(9\text{Cr}) = C_{\text{Cr}}(\text{Inner Spinel Oxide}) * [V(\text{Inner Spinel Oxide}) - V(\text{void})] \tag{E2}$$

with $V(9\text{Cr})$, $V(\text{Inner Spinel Oxide})$, $V(\text{Fe}_3\text{O}_4)$ and $V(\text{void})$ the volumes of the consumed metallic substrate, of the inner spinel oxide layer, of the outer magnetite layer and the of the voids, respectively. The quantities $C_{\text{Cr}}(9\text{Cr})$ (0.013 mol/cm^3), $C_{\text{Fe}}(9\text{Cr})$ (0.12 mol/cm^3), $C_{\text{Cr}}(\text{Inner Spinel Oxide})$, $C_{\text{Fe}}(\text{Inner Spinel Oxide})$ and $C_{\text{Fe}}(\text{Fe}_3\text{O}_4)$ (0.067 mol/cm^3), are the chromium and iron concentration in 9Cr steel, the chromium concentration and the iron concentration in the inner Fe–Cr spinel oxide and in magnetite, respectively. The void fraction, $f(\text{void})$, was obtained by dividing (E1) by (E2). The following expression E3 was obtained in one space dimension:

$$f(\text{void}) = 1 - \frac{1}{\left(\frac{C_{\text{Fe}}(9\text{Cr})}{C_{\text{Cr}}(9\text{Cr})} - \frac{C_{\text{Fe}}(\text{Inner Oxide Spinel})}{C_{\text{Cr}}(\text{Inner Oxide Spinel})} \right) * \left(\frac{C_{\text{Cr}}(\text{Inner Oxide Spinel}) * h(\text{Inner Spinel Oxide})}{C_{\text{Fe}}(\text{Fe}_3\text{O}_4) * h(\text{Fe}_3\text{O}_4)} \right)} \quad (\text{E3})$$

with $h(9\text{Cr})$, $h(\text{Inner Spinel Oxide})$ and $h(\text{Fe}_3\text{O}_4)$, the thicknesses of the consumed metallic substrate, the inner spinel oxide layer and the outer magnetite layer, respectively. The molar concentrations of Cr and Fe in the oxide are related to the oxide stoichiometry through the following relations:

$$C_{\text{Cr}}(\text{Inner Oxide Spinel}) = \frac{x}{V_{\text{Fe}_{3-x}\text{Cr}_x\text{O}_4}} \quad (\text{E4})$$

$$C_{\text{Fe}}(\text{Inner Oxide Spinel}) = \frac{3-x}{V_{\text{Fe}_{3-x}\text{Cr}_x\text{O}_4}} \quad (\text{E5})$$

With $V_{\text{Fe}_{3-x}\text{Cr}_x\text{O}_4}$, the molar volume of the Fe–Cr spinel oxide taken equal to the one of Fe_3O_4 , $44.7 \text{ cm}^3/\text{mol}$ and x , the stoichiometric coefficient of the inner spinel oxide scale. Thus, Expression (E3) is re-written as:

$$f(\text{void}) = 1 - \frac{1}{\left(\frac{0.12 \text{ mol cm}^{-3}}{0.013 \text{ mol cm}^{-3}} - \frac{3-x}{x} \right) * \left(\frac{x}{3} * \left(\frac{h(\text{Inner Spinel Oxide})}{h(\text{Fe}_3\text{O}_4)} \right) \right)} \quad (\text{E6})$$

According to (E6), the fraction of voids in the inner spinel oxide layer is directly linked to the composition of the inner spinel oxide layer (x value) and the ratio of the inner/outer oxide thicknesses, $\left(\frac{h(\text{Inner Spinel Oxide})}{h(\text{Fe}_3\text{O}_4)} \right)$.

The average experimental x value was determined from the %at Cr and %at Fe in the inner spinel layer measured by EDS-TEM on many zones (Fig. 14) and the following expression E7:

$$\left(\frac{\% \text{at Cr}}{\% \text{at Fe}} \right)^{\text{exp}} = \frac{x}{3-x} \quad (\text{E7})$$

From Fig. 14, $x \approx 1.2$ and the ratio of the inner/outer oxide thickness, $\left(\frac{h(\text{Inner Spinel Oxide})}{h(\text{Fe}_3\text{O}_4)} \right)$ is equal to 1/3 (200 nm/600 nm). With all the uncertainties on measurement of the oxide thicknesses, % at Cr, % a Fe and by considering a few large pores as well in magnetite, it was calculated that $3\% < f(\text{void}) < 12\%$. The experimental value of $f(\text{void})$ determined by image analysis in Fig. 15 was about 8–9%. This experimental void fraction value is in satisfactory agreement with the value expected from expression (E6).

It is to be noted that the relative thicknesses of the inner and outer oxide layers are not as expected. In longer term experiments the ratio of the inner to outer layer thicknesses is 1.1 and the average inner layer stoichiometry expressed by x has the value 0.6. It can be concluded that during the first 20 min of oxidation, the steady state has not yet been reached.

Once the formation of the duplex oxide scale had started, that is to say with an outer iron oxide layer (magnetite or hematite or both) and a mixture of Fe_3O_4 , Cr

rich Fe–Cr spinel and gas-filled pore space, its growth rate was controlled by diffusion through the scale which in term depends upon the oxygen potential at the gas–oxide interface and diffusion of iron through the scale. One difficulty is to know, at any time, the exact oxygen potential at the gas–oxide interface, that is to say the concentration of adsorbed oxygen atoms free to react with the substrate to form oxide. As mentioned previously, this value depends strongly on kinetics factors such as the impingement rate of the molecules, their dissociative adsorption rate and the rate of reaction with other adsorbed molecules on the surface such as CO. In 49 CO₂–O₂, during the first fifteen minutes when O₂ is still present in the reactor, the minimum oxygen potential imposed at the substrate surface is greater than the one imposed by pure CO₂.

After the fifteen minutes long period, when all O₂ molecules in the reactor were consumed, CO was produced (no recombination with O₂ to form CO₂ being possible) and accumulated in the reactor. Thus, the oxidizing potential at the gas–oxide surface was established by a CO/CO₂ gas mixture. With increasing CO pressure, the oxygen potential decreased drastically (Fig. 32). Therefore, the oxide growth rate decreased drastically as illustrated by Figs. 26. The presence of magnetite and absence of hematite at the oxide–gas interface after the test was in good agreement with the thermodynamic prediction in CO/CO₂ gas mixture (Fig. 33).

When the O₂ pressure in CO₂ was instead 5 mbar (test in 49CO₂–5O₂), the initial high oxide growth rate did not decrease drastically at $t \approx 15$ min because O₂ molecules were still present. The formation of a CO₂/CO environment was postponed and, consequently, the high oxidation rate was maintained (Figs. 19 and 20). However, it decreased progressively with time. This observation could be explained by the progressive decrease of P_{O_2} in the reactor or more likely by the fact the rate limiting step of oxide growth switched from the dissociation rate of O₂ molecules to the diffusion of iron cations which also depends on P_{O_2} , but to a lesser extent. Indeed, in 49CO₂–5O₂, O₂ was totally consumed and CO molecules started to be produced at $t \approx 140$ min (Fig. 16) but this event did not have a drastic influence on the oxidation rate as was the case in 49CO₂–1O₂. This last scenario was suggested to occur for iron and mild steel in CO₂/O₂ gas mixtures when the thickness of magnetite reached about 1.2 μm [10].

Corrosion Behavior in O₂ and in CO₂ with High Pressure of O₂

Corrosion Behavior in pure O₂

As proposed in the previous part d.ii), the activation of the fast oxidation/carburization behavior mode of 9Cr steel in CO₂–O₂ gas mixture is induced by a high initial surface oxygen potential which causes a high initial oxidation rate of iron (very likely rate limited by O₂ dissociation as evidenced in [10] for iron), formation of high concentrations of iron vacancies which condenses into voids, which make inward transport through the inner layer possible. On this basis, the oxidation behavior of 9Cr steel in pure O₂ would be expected to operate as in CO₂–O₂ gas

mixture since the oxidizing power of O_2 is even larger than in CO_2 – O_2 environments (Fig. 32).

To some extent, this was the case: A duplex scale made of an outer iron oxide and an inner chromium-iron-rich oxide formed without any Cr depletion in the metallic substrate below the oxide scale (Figs. 24 and 25). Thus, the morphology of the oxide scale was close to the one formed in CO_2 – O_2 environments on some parts of the surface (“thick” oxide scale”, Fig. 24), but differed on other parts which developed a much thinner chromium-rich oxide scale (“thin” oxide scale, Fig. 25). By looking carefully on the morphology and the composition of the oxide scale, it could be noted that, after exposure in 1 mbar O_2 , a gap is observed in between the oxide scale and the substrate (Fig. 25). It is not clear from the available evidence whether this gap is due to vacancies created by oxidation or simply scale/metal mechanical separation. Moreover, the chromium concentration in the inner spinel oxide was much higher than after exposure in CO_2 – O_2 forming an average stoichiometry of $FeCr_2O_4$ or even richer in chromium, to be compared with $Fe_{1.8}Cr_{1.2}O_4$ in $49CO_2$ – $1O_2$. This higher concentration in chromium after exposure in pure O_2 could be explained according to the ASM. Indeed, at 550 °C, chromium atoms are almost immobile [18] and the chromium concentration in the inner oxide layer is, according to the ASM, a consequence of iron depletion due to outwards iron oxide growth mainly. Since faster outward growth of iron oxide occurred in pure O_2 , more depletion of iron would occur at the oxide/metal interface.

Except during the first minutes of exposure, the observed oxide growth rate was much lower in pure 1 mbar O_2 than in 49 mbar CO_2 —1 mbar O_2 (Fig. 26). The reasons for this beneficial effect of O_2 on the oxidation rate of 9Cr steel are of obvious interest and is discussed. There are three factors that lead to slower oxidation rate. Firstly, the continuous Cr-rich inner oxide layer slows transport of iron. As a result of the slowed transport of iron, magnetite is transformed into hematite. Hematite could have been formed without any need of the formation of inner chromium-rich oxide layer and only because of the higher oxidizing potential of pure O_2 (Fig. 32). The presence of hematite could have decreased the oxidation rate as well. And finally, the oxidation rate could have decreased drastically because of the separation of metal and oxide in many parts of the surface.

Very interestingly, Fig. 26 shows that the rate of oxidation of iron, mild steel and 9Cr in 1 mbar O_2 was equal within the first minute of exposure but then was much higher for iron and mild steel. Since the impingement rate of O_2 and the dissociation rate of O_2 are assumed to be equal for the tests on iron/mild steel and 9Cr steel, it is expected that the oxidation rate would be the same for the three alloys. This is exactly what was observed within the first minute of exposure. But the consequence of this very fast oxidation rate differed strongly between iron/mild steel and 9Cr steel in the following minutes of exposure. In the latter case, the fast oxidation of Fe led to Cr enrichment in the inner layer, consequent formation of a Cr-rich inner oxide layer and separation of the oxide and the metal in many parts of the surface. Iron and mild steel succeeded in maintaining a good oxide/metal adhesion, probably by moving the oxide-metal interface more easily (better plasticity of the oxide). The formation of voids at the oxide/metal interface may be strongly linked to the ability

of the substrate to annihilate metal vacancies, as proposed by Gibbs [16], Robertson et al. [18] and Atkinson et al. [19].

Corrosion Behavior in CO₂ with High pressure of O₂

When the O₂/CO₂ ratio in the gas environment was increased, the oxygen potential on the surface is increased and the formation of hematite is favored from the very first instants of exposure on some parts of the sample: some parts of the surface are covered by “O₂ like” protective oxide scale and some other parts by “CO₂ like” non-protective oxide scale. The surface fraction of the protective oxide scale increased with the O₂/CO₂ ratio in the gas mixture.

Influence of H₂O in CO₂–O₂

The reactivity of 9Cr in CO₂–O₂–H₂O gas mixtures was very similar to what has been observed in CO₂–O₂ gas mixtures (part 3 b)).

First, a thick iron-rich duplex oxide scale formed on the surface of 9Cr steel, with the same structure and morphology as the one formed in CO₂/O₂ gas mixture. This observation is in agreement with a previous study [24].

Secondly, the GPA showed that all molecules, O₂, H₂O and CO₂ participated to the oxide growth. Similar reactions between atoms and molecules than the ones observed in CO₂–O₂ gas mixtures occurred on 9Cr surface. The O₂ molecules dissociated fast on the surface and the produced ¹⁸O atoms recombined, not only with CO to form ¹³C^{18,16}O₂, as it was the case in CO₂–O₂ gas mixtures, but with H₂ coming from H₂O dissociation as well to form ²H₂¹⁸O, respectively. Interestingly, less produced H₂ than CO molecules recombined with ¹⁸O atoms, whereas both initial H₂O and CO₂ pressures were equal, 10 mbar (Fig. 27). This observation could be explained by the more reducing power of CO than H₂. Indeed, the equilibrium constant of dissociation of CO₂ (to form 0.5O₂ and CO) is about 4 times higher than H₂O (to form 0.5O₂ and H₂). They were calculated to be 4.1 10^{–14} bar and 1.4 10^{–13} bar, respectively, at 550 °C [25].

H₂ and CO molecules were also produced during 9Cr oxidation in 10CO₂–0.5O₂–xH₂O gas mixtures even when O₂ was present in the reactor. This observation differed with what was observed in 49CO₂–1O₂ where no CO was produced. This difference were very likely due to the lower O₂ pressure in the used gas mixtures which disfavored the recombination of all produced CO and H₂ molecules. The much higher rate of O₂ consumption than CO and H₂ production confirmed that O₂ was the main oxidizing species during the growth of the transient oxide scale in initial stages of exposure. When O₂ was totally consumed in the reactor, the molecules that participated to the growth of the oxide layers was H₂O and CO₂ with the production of H₂ and CO.

Finally, adding H₂O in CO₂–O₂ has a strong impact regarding carburization. The carburization rate of 9Cr steel decreased with the increase of P_{H₂O}/P_{CO₂}

pressure in the gas mixture. This important phenomenon has already been evidenced on 9Cr steel by Abellan et al. at 550 °C [8] and Gheno et al. at 650 °C [9]. In the ASM, it is proposed that the oxidizing molecules such as O₂, H₂O and of course CO₂ diffuse through the oxide scale via “high diffusion pathways” such as cracks to reach the oxide-metal interface. For Ni, Atkinson demonstrated that these cracks are formed in oxide grain boundaries preferentially [19]. Then, these oxidizing molecules react with the metallic elements present on the surface of the voids. The reaction of CO₂ with the metallic elements produces CO molecules which then induces carburization through the Boudouard reaction. To explain the beneficial influence of water molecules against carburization, it is proposed that H₂O preferentially adsorbs on the surface of the voids and limits CO₂ and/or CO reaction. Indeed, Anghel et al.’s has demonstrated that H₂O molecule has a much stronger adsorption power than O₂ and other molecules such as N₂, H₂ or CO [26]. The preferential adsorption of H₂O over CO has also been demonstrated in [27]. Since we have demonstrated that O₂ react preferentially to CO₂, it is justified to propose that CO₂ has a much lower adsorption power than H₂O as well. The fact that hydrogen was massively detected in the inner Fe–Cr spinel layer are in good agreement with this scenario of CO₂/H₂O adsorption competition. This region was exactly where was observed the accumulation of carbon after exposure to CO₂/O₂ gas mixture. In consequence, it could be proposed that the hydrogen accumulation was provoked by the reaction of the water molecules in the inner layer during the ASM. Once transferred in the oxide scale, hydrogen accumulated, then, in the Cr-rich oxide region and not the iron-rich oxide, very likely due to its higher affinity with chromium than with iron [28]. The absence of H in the outer magnetite layer might also be explained by the fact that magnetite grows at the gas/oxide interface and, in consequence, the produced H₂ molecules desorb into the gas phase favorably.

Conclusions

The following conclusions can be proposed for this study:

- The corrosion behavior of 9Cr steel in CO₂/O₂/H₂O gas mixtures at 550 °C was analyzed by gas phase analysis using isotopic molecules in order to probe all gas–gas and gas–solid reactions.
- All molecules, CO₂, H₂O and O₂, reacted with the 9Cr surface to form a transient oxide scale.
- The composition and structure of the transient oxide scale was determined by the *surface reaction rate* of 9Cr steel at the very beginning of the test, during the first minutes of exposure.
- The formation rate of the transient oxide scale was clearly controlled by the rate at which the gas phase supplies adsorbed oxygen atoms, and in consequence, depends strongly on the partial pressure of O₂.

- In pure CO₂, 9Cr oxide steel formed a slow growing oxide scale with a Cr rich oxide due to the low oxidizing power of CO₂.
- In CO₂ containing a low amount of O₂, the oxidation rate of 9Cr was drastically increased by the high oxidizing power of O₂ molecules. In CO₂/O₂ gas mixture, almost all oxygen atoms created by the dissociation of O₂ on the surface recombined with the formed CO molecules created by CO₂ dissociation to form again CO₂ molecules. The oxidation rate was strongly increased compared to pure CO₂. Only the use of labelled molecules could demonstrate this non obvious reaction scheme. In that gas mixtures, fast growing duplex iron-rich oxide scale formed with a microstructure consistent with the “Available Space Model”, accompanied by strong carburization.
- In pure O₂, the oxidizing power of the gas is even more increased, and a thin duplex oxide scale made of inner chromium very rich oxide and outer hematite is formed. Oxidation was, initially, much faster than in the CO₂/O₂ gas mixtures, in agreement with the faster supply of adsorbed oxygen atoms, but was stopped very quickly. The slower rate could be explained by the separation of the oxide scale from metal and/or the formation of outer hematite and inner chromium-rich oxide layer that both decreased iron diffusion.
- In CO₂ containing a high amount of O₂, thin and thick duplex oxide scales, such as the one observed in pure O₂ and in CO₂ with low amount of O₂, were formed.
- The oxidation behavior of 9Cr observed in H₂O containing CO₂/O₂ gas mixtures was similar to CO₂ containing low amount of O₂ gas mixtures with a quite similar reaction scheme on the surface, but less carburization.
- Adding H₂O to carburizing CO₂/O₂ gas mixtures decreased the carburization rate of 9Cr steel and transferred hydrogen into the inner Cr-rich oxide layer. The carburization rate decreased with the increase of H₂O/CO₂ ratio in the gas mixture. These observations were very likely due to the strong adsorption of some H₂O-derived species in the inner oxide layer.

Acknowledgements The authors are grateful to Ms R. Benyhia for carrying out part of the oxidation tests during their Master internship, Mr M. Tabarant for the GDOES analyses and Mr Schlegel for the Raman analyses.

Authors Contributions Conceptualization: F.R.; Methodology: F.R.; Formal analysis and investigation: F.R, F.J, L.L-R, F.M, L.M, D.J.Y; Writing—original draft preparation: F.R, L.L-R, L.M, D.J.Y; Funding acquisition: F.R; Resources: F.R; Supervision: F.R.

Funding This study was funded by the French Alternative Energies and Atomic Energy Commission.

Data Availability The raw/processed data required to reproduce these findings can be shared if necessary.

Declarations

Competing interests The authors declare no competing interests.

Conflict of interest The authors declare that they have no conflict of interest.

References

1. R. Oleksak and F. Rouillard, in *Materials Performance in CO₂ and Supercritical CO₂. Comprehensive Nuclear Materials*, 2nd edition, Vol. 4 (Elsevier, 2020), p. 422.
2. S. Bouhieda, F. Rouillard, V. Barnier, and K. Wolski, *Oxidation of Metals* **80**, 2013 (493).
3. S. Bouhieda, F. Rouillard, and K. Wolski, *Materials at High Temperature* **29**, 2011 (151).
4. G. H. Meier, K. Y. Jung, N. Mu, et al., *Oxidation of Metals* **74**, 2010 (319).
5. J. P. Abellan, T. Olszewski, G. H. Meier, et al., *International Journal of Materials Science* **101**, 2010 (287).
6. W. J. Quadackers, T. Olszewski, J. P. Abellan, et al., *VDI-Berichte* **2012**, 2010 (81).
7. D. Huenert and A. Kranzmann, *Corrosion Science* **53**, 2011 (2306).
8. J. P. Abellan, T. Olszewski, G. H. Meier, L. Singheiser, and W. J. Quadackers, *International Journal of Materials Research* **101**, 2010 (287).
9. T. Gheno, D. Monceau, and D. J. Young, *Corrosion Science* **77**, 2013 (246).
10. F. Rouillard and D. J. Young, *Corrosion Science* **178**, 2021 109092.
11. E. F. Rauch and M. Véron, *Materials Characterization* **98**, 2014 (1).
12. F. Rouillard, G. Moine, L. Martinelli, and J. C. Ruiz, *Oxidation of Metals* **77**, 2012 (27).
13. I. Wolf, H. J. Grabke, and P. Schmidt, *Oxidation of Metals* **29**, 1988 (289).
14. F. Rouillard and T. Furukawa, *Corrosion Science* **105**, 2016 (120).
15. F. Rouillard, G. Moine, M. Tabarant, and J. C. Ruiz, *Oxidation of Metals* **77**, 2012 (57–70).
16. G. B. Gibbs, *Oxidation of Metals* **7**, 1973 (173).
17. R. P. Oleksak, M. Kapoor, D. E. Perea, G. H. Holcomb, and O. N. Dogan, *npj Materials Degradation* **2**, 2018 (25).
18. J. Robertson and M. I. Manning, *Materials Science and Technology* **4**, 1988 (1064).
19. A. Atkinson and D. W. Smart, *Journal of the Electrochemical Society* **135**, 1988 (2886).
20. L. Martinelli, F. Balbaud-Célérier, A. Terlain, et al., *Corrosion Science* **50**, 2008 (2537).
21. T. Gheno, D. Monceau, J. Zhang, and D. J. Young, *Corrosion Science* **53**, 2011 (2767).
22. D. J. Young, P. Huczowski, T. Olszewski, et al., *Corrosion Science* **88**, 2014 (161).
23. K. E. Nygren, Z. Yu, F. Rouillard, and A. Couet, *Corrosion Science* **163**, 2020 108292.
24. L. Martinelli, C. Desgrange, F. Rouillard, et al., *Corrosion Science* **100**, 2015 (253).
25. HSC Thermochemistry[®] software version 10.3.4, Metso Outotec Finland Oy.
26. C. Anghel, E. Hornlünd, G. Hultquist, and M. Limbäck, *Applied Surface Science* **233**, 2004 (392).
27. J. Chapovaloff, F. Rouillard, K. Wolski, and M. Pijolat, *Corrosion Science* **69**, 2013 (31).
28. G. Hultquist, M. J. Graham, J. L. Smialek, and B. Jönsson, *Corrosion Science* **93**, 2015 (324).

Publisher's Note Springer Nature remains neutral with regard to jurisdictional claims in published maps and institutional affiliations.

Springer Nature or its licensor (e.g. a society or other partner) holds exclusive rights to this article under a publishing agreement with the author(s) or other rightsholder(s); author self-archiving of the accepted manuscript version of this article is solely governed by the terms of such publishing agreement and applicable law.

Authors and Affiliations

F. Rouillard¹ · F. Jomard² · L. Latu-Romain³ · L. Martinelli¹ · F. Miserque¹ · D. J. Young⁴

✉ F. Rouillard
fabien.rouillard@cea.fr

¹ CEA, Service de Recherche en Corrosion et Comportement des Matériaux, Université Paris-Saclay, 91191 Gif-sur-Yvette, France

- ² Univ Versailles St Quentin En Yvelines UVSQ, Grp Etud Matiere Condensee GEMaC UMR8635, CNRS,, Univ Paris Saclay, 45 Av Etats Unis, 78035 Versailles, France
- ³ Ugitech Res Ctr, Ave Paul Girod, 73403 Ugine, France
- ⁴ School of Materials Science and Engineering, University of New South Wales, Sydney, NSW 2052, Australia